JOURNAL OF GEOPHYSICAL RESEARCH, VOL. 105, NO. B6, PAGES 13,281–13,301, JUNE 10, 2000

Fold style inversion: Placing probabilistic constraints on the predicted shape of blind thrust faults

Benjamin A. Brooks,[1] Eric Sandvol, and Andrew Ross[2]

Institute for the Study of the Continents, Department of Geological Sciences
Cornell University, Ithaca, New York

Abstract. We develop a new methodology which compares quantitatively styles of folding from seismic reflection data. The goal of the "fold style inversion" (FSI) method is to provide an objective choice of the most appropriate model used when solving for the shape of an unimaged blind fault from folded layer geometry. FSI is a discretization of the dip isogon fold classification scheme reformulated as simple vector transformations. A data set's goodness of fit to parallel (class 1c) or similar (class 2) fold geometry is assessed by calculating misfit between the predicted and observed bed geometries through a grid search of the parameter space specific to each transformation; the two fold types correspond to the constant bed length and arbitrarily inclined simple shear (AISS) fault solution routines, respectively. For seismic reflection data, confidence estimates may be placed on the preference of fold style and its corresponding fault solution by Monte Carlo simulations of depth correlative, spatially limited depth conversion errors. For synthetic geometric examples FSI determines fold style preference and parameters exactly. At low fold limb dips (<~15°) the actual geometric difference between parallel and similar folds is very small, and the difference between fold styles cannot be resolved, highlighting a general difficulty in the analyses of young blind thrust structures. For a synthetic seismic line of an AISS fault-related fold the method chooses the correct folding style and leads to the correct fault geometry at depth. In examples of real data from the Barrancas/Lunlunta-Carrizal anticlinal complex in Mendoza, Argentina, FSI analysis determines 71% and 54% probability of similar preference for two seismic lines on separate structures. The corresponding fault solutions for the first example are well constrained, whereas for the second example the solutions are widely variant. This analysis helps to quantify the relationship between the predicted sub surface fault trajectories and hypocenter and aftershock data of the 1985 M_w 5.9 Mendoza earthquake, showing that the earthquake and the fault causing the Barrancas/Lunlunta-Carrizal anticlinorium are most likely unrelated.

1. Introduction

Determining the subsurface geometry of "blind" thrust faults is fundamental to any active tectonic or seismic hazard analyses of these potentially seismogenic structures. Where anticlinal folds overlying blind thrust faults have been explored for hydrocarbon reserves, industry seismic reflection lines commonly provide the most complete and highest-quality spatial data. Frequently, however, the seismic reflection data only image the folded layers, while the potentially seismogenic fault remains hidden. As a result, the depth profile of a buried fault is often estimated from the geometry of the overlying folded rock layers through some kinematic model which relates incremental fault slip to permanent fold deformation [*Erslev*, 1991; *Suppe*, 1983; *Suppe and Medwedeff*, 1990; *White et al.*, 1986]. It is this modeled fault geometry which is then used in determining slip rates, potential earthquake magnitudes, and recurrence intervals or, recently, in correlating the relocated hypocenter of an earthquake with fault plane reflections below a surficial fold [*Shaw and Shearer*, 1999].

Because of the variety of models relating fold shape to fault shape and slip, modeled subsurface fault trajectories may be highly nonunique. For instance, for the same folded layer geometry, the arbitrarily inclined simple shear (AISS) and constant bed length (CBL) fault solution routines may yield significantly different fault trajectories (Figure 1) [*Dula*, 1991]. While corollary geologic data such as growth strata packages may be used to deduce time-averaged fold kinematics and to choose the most appropriate fault-related fold model, these data often do not exist, especially in subaerial locations where sedimentation rates are lower. As a result, workers often choose a fault-related fold model to apply on the basis of subjective criteria such as ease of graphical implementation, computer code availability, or personal preference. Given that these fault solutions are often used in seismic hazard analyses with direct societal impact, an objective criterion to choose the fault-related fold model most appropriate to a data set would be extremely useful.

In this paper, we develop a method to allow an objective choice of the most appropriate fault-related fold model to use when solving for the shape of an unimaged fault from seismic

[1]Now at Hawaii Institute for Geophysics and Planetology, School of Ocean and Earth Science and Technology, Honolulu.
[2]Now at Geologisk Institut, Copenhagen, Denmark.

Paper number 2000JB900044.
0148-0227/00/2000JB900044$09.00

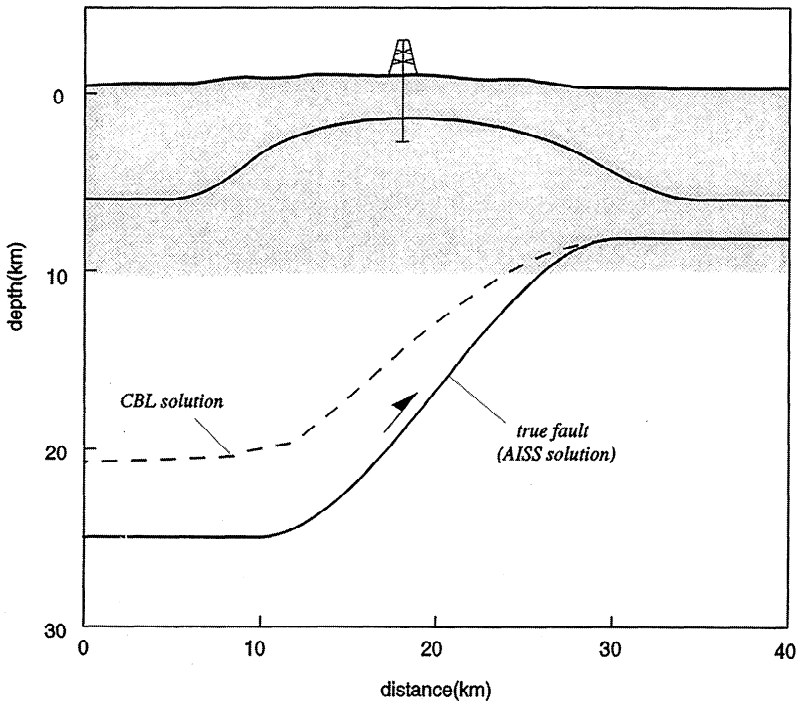

Figure 1. Cross-sectional view of an AISS fault bend fold forward model (solid line) and the constant bed length (CBL) fault solution (dashed line) obtained from the folded layer. If the AISS fault solution routine had been used, the exact trajectory of the true fault would have been obtained. The gray area indicates the maximum depth of typical industry seismic reflection lines.

reflections of folded layers. The "fold style inversion" (FSI) method compares quantitatively the style of folding which best corresponds to folded layer geometry imaged in seismic reflection data. In our development, we explicitly consider depth conversion errors that may influence the final geometry of reflections in standard common midpoint (CMP) seismic reflection profiles. Iterative Monte Carlo simulations of these errors allow confidence estimates to be placed on the choice of a specific model and its corresponding fault solution. In addition to tests on kinematic forward models, we test the FSI method on a synthetic CMP profile and apply it to an active fault-related fold, the Barrancas/Lunlunta-Carrizal anticlinal complex, situated near a densely populated area in Argentina's eastern Andean foothills and the site of the 1985 $M_W = 5.9$ Mendoza earthquake.

2. Fold Style Inversion

Generally, the method is a grid search of a parameter space specific to a fold style for a bulk fold geometry which minimizes the error produced when folded reference layers are spatially transformed into model layers. The overall goal is to choose the most appropriate model describing fault-related fold deformation. This preferred model is then used to invert hanging wall fold geometry for fault geometry at depth.

We present the method below in four components: (1) a transformation of points from a reference to a model layer using a discrete formulation of the dip isogon fold classification scheme [*Hudleston*, 1973; *Ramsay*, 1967], (2) a grid search of a parameter space specific to each transformation and error minimization between modeled and actual layers, (3) Monte Carlo simulation of a depth-correlative error function which replicates ray-path-dependent depth conversion errors, and (4) inversion for fault geometry given deformed hanging wall layer geometry.

In the subsequent development, we consider only two-dimensional, plane strain deformation and choose only two fault solution routines, the AISS [*Kerr et al.*, 1993] and CBL [*Geiser et al.*, 1988] methods, which correspond to arbitrarily inclined simple shear and layer parallel shear (LPS) deformation mechanisms, respectively (see the appendix for a more detailed description of these deformation mechanisms and fault solution routines). We fully recognize that deformation is three dimensional [*Kerr et al.*, 1993; *Unruh and Twiss*, 1998] and may not be described as simply as the models we choose. However, in order to present clearly the method and to understand its first-order results, we have made the above limiting assumptions which are standard in geologic cross-section construction [*Woodward et al.*, 1989]. Furthermore, we choose the AISS and CBL methods because they are two widely employed inverse methods relating fold geometry to fault geometry [*Geiser et al.*, 1988; *Suppe*, 1983; *Suppe and Medwedeff*, 1990; *White et al.*, 1986] and because the fold kinematics specific to each method are correlated with unique fold styles defined by the dip isogon classification.

2.1. Discretized Dip Isogon Classification

Each particular style of fault-related folding has a unique geometrical relationship between folded layers. These geometrical relationships may be visualized graphically as fold classes defined by dip isogons, lines connecting layer segments of equivalent dip [*Elliot*, 1965; *Hudleston*, 1973; *Ramsay*, 1967] (Figure 2) LPS deformation will form "parallel," or class 1B, folds. AISS deformation will form "similar," class 2, folds [*Ramsay*, 1967]. The dip isogon

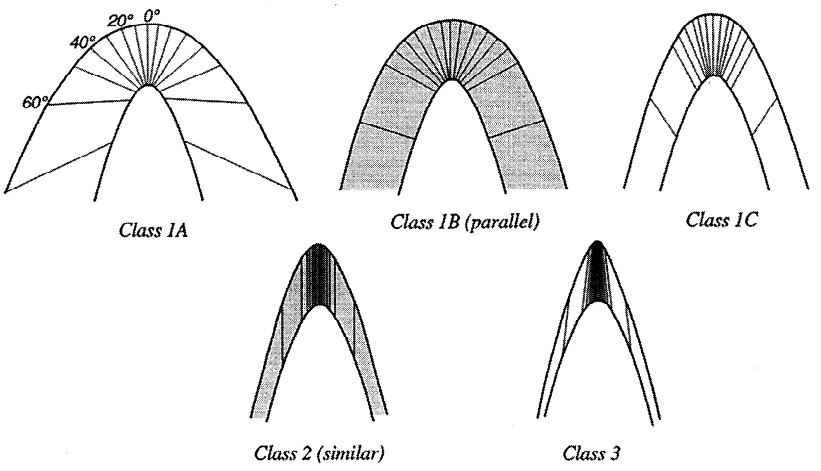

Figure 2. The five possible fold classes in the dip isogon classification [*Ramsay*, 1967]. Dip isogons are lines which connect regions of equivalent dip between folded layers. At this stage we only consider the parallel (class 1B) and similar (class 2) categories which correspond to the CBL and AISS fault solution routines, respectively.

classification is an entirely general scheme; all simple fold types fall into one of five categories (Figure 2).

We describe the dip isogon geometrical relationships as a transformation of points on a reference layer to points on a model layer. In a two-dimensional coordinate system with $\boldsymbol{i}$ and $\boldsymbol{j}$ as horizontal and vertical unit vectors along the x and y axes, respectively, the material points of layers in a similar fold, the result of AISS deformation, may be related to one another as follows (Figure 3a):

$$\mathbf{b}(x) = \mathbf{a}(x) + t_{ax}\mathbf{v}, \tag{1}$$

where $\mathbf{a}(x)$ is the vector from the origin to a point on the reference layer (the ith layer in any set of layers), $\mathbf{b}(x)$ is the vector from the origin to the same point on the model layer, t_{ax} is the axial planar thickness of the similar fold, $\mathbf{v}$ is a unit vector, and $\mathbf{v} \cdot \mathbf{j} = \cos(\alpha)$, where α is the angle of inclined simple shear [*White et al.*, 1986]. When $\mathbf{v}$ is rotated counterclockwise from the vertical, $\alpha > 0$; when $\mathbf{v}$ is rotated clockwise from the vertical, $\alpha < 0$. Likewise, the material points of layers in a parallel fold, the result of LPS deformation, may be related to each other as

$$\mathbf{b}(x) = \mathbf{a}(x) + t_{perp}\mathbf{v}_{perp}(x), \tag{2}$$

where $\mathbf{a}(x)$ and $\mathbf{b}(x)$ are defined in the same way as equation (1), t_{perp} is the layer perpendicular thickness, and $\mathbf{v}_{perp}(x)$ is a unit vector perpendicular to the layer at each point on the reference layer (Figure 3b); $\mathbf{v}_{perp}(x)$ is a function of x, and its orientation varies accordingly, while $\mathbf{v}$ in equation (1) has a constant orientation.

2.2. Grid Search and Misfit Calculation

Although simple, equations (1) and (2) cannot be represented in explicit linear form [*Menke*, 1984]. Accordingly, we cannot perform a simple linear inversion to find the bestfitting parameters, α, t_{ax}, and t_{perp} from equations (1) and (2). Instead of making potentially complicated linearizing assumptions and because reasonable bounds on the parameters are limited and easy to define, we choose to find the best fitting parameters by means of a grid search of the solution space [e.g., *Sambridge and Kennett*, 1986]. The grid search approach allows evaluation of the convergence strength and uniqueness of solutions by direct observation and guarantees determination of the global minimum.

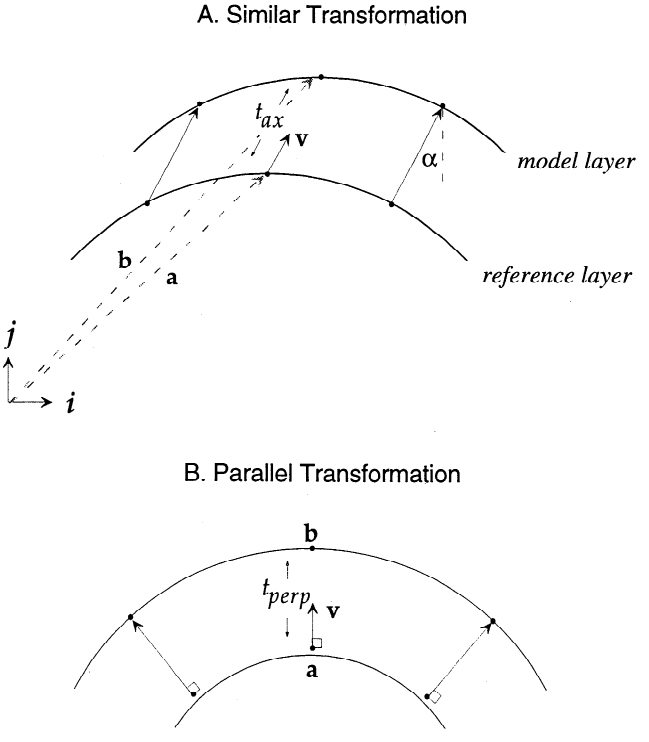

Figure 3. (a) Transformation of points from reference layer (points **a**) to model layer (points **b**) according to similar fold geometry. All points are translated along a vector **v** for a distance t_{ax} and deviate from the vertical by α in a coordinate system defined by unit vectors **i** and **j**. If rotated counterclockwise, $\alpha > 0$; if rotated clockwise, $\alpha < 0$. (b) Transformation of points according to parallel fold geometry. Points are translated along **v** for a distance t_{perp} in an orientation which is always perpendicular to the local bedding.

Simple similar folding (AISS deformation) has a two-dimensional parameter space consisting of parameters α and t_{ax} (equation (1)) while simple parallel folds (LPS deformation) are described by only one parameter, t_{perp} (equation (2)). In practice, we substitute for t_{ax} and t_{perp} a reference thickness t_{ref}, expressed as a percentage of the average layer perpendicular thickness between two layers. The parameter varied in the grid search is then t_{ref}. To illustrate the method in a simple way, we do not consider other possible parameters such as porosity decay length [*White*, 1987] or degree of homogenous shear imposed over the hanging wall [*Mosar and Suppe*, 1992], though they may be added eventually.

For a given set of digitized layers, the grid search comprises computing the misfit ε between modeled and actual data for each possible combination of model parameters specific to a deformational style. We choose an L_2 norm [*Menke*, 1984], and for any pair of layers with points $\mathbf{a}(x)$ and $\mathbf{b}(x)$ from (1) or (2) we define

$$\varepsilon_{ab} = \frac{\left[\sum_{i=1}^{N_b} \left(\hat{y}_{bi} - y_{bi}\right)^2\right]^{1/2}}{N_b}, \quad (3)$$

where y_{bi} is the vertical coordinate of the ith point on the second digitized layer, $\hat{y}_{bi}$ is the vertical coordinate of the modeled data which shares the same horizontal coordinate with y_{bi}, and N_b is the total number of points on the second layer (Figure 4). Equation (3) is calculated for each pair of layers and then summed to find the total of the average misfit per point specific to a set of layers. If L is the total number of layers in a set, then there are L $(L\text{-}1)$ combinations to which we apply (3) and we define the total misfit ε_{tot} as

$$\varepsilon_{tot} = \sum_{j=1}^{L} \sum_{k=1}^{L} \varepsilon_{jk(j\neq k)}. \quad (4)$$

For data where measurement uncertainties may be estimated directly, such as rock outcrop or sandbox models, the preferred model parameters simply would correspond to the smallest value of ε_{tot} within the range of uncertainty. For seismic reflection images, however, uncertainty estimation is much more complicated. Errors may enter the data set anywhere along the path from field acquisition to processing and depth conversion. To insure quantitative validity of the method, we address below the uncertainties specific to seismic reflection data and how they may influence our analysis.

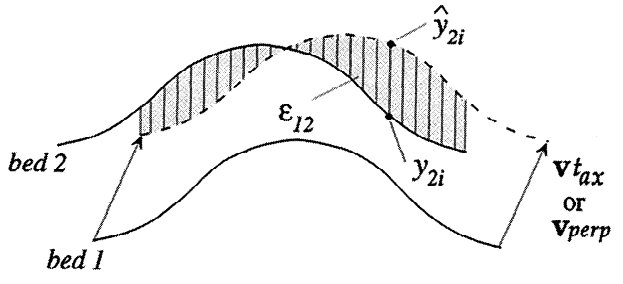

Figure 4. Misfit calculation for a representative pair of beds. For each pair of beds, misfit is calculated following equation (3) for each point transformed according to equations (1) and (2).

The primary goal of the grid search and misfit calculation is to identify which fold model is most suitable to the data; additionally, the estimated parameter α will be used in subsequent analysis. Primarily, α, the angle of inclined simple shear, is the controlling variable in the AISS fault solution routine [*White et al.*, 1986] (see the appendix). We are not as concerned with the actual values of the thickness parameters t_{ref} and t_{ax} in each vector transformation because these parameters do not enter into subsequent fault inversion routines.

2.3. Synthetic Examples: Kinematic Models

Using synthetic examples of AISS and LPS forward models, we illustrate the grid search and misfit calculation when experimental uncertainties are not present in the data. Figure 5a is an example of beds folded according to AISS deformation in response to slip on an underlying thrust fault with a flat-ramp-flat ("fault bend fold") geometry and α = -20° inclined synthetic to the fault ramp. The one parameter parallel grid search (equation (2)) clearly converges to a global minimum of ε_{tot} ~ = 4 m at t_{ref} = ~100% (Figure 5b). The contoured error surface of the two-parameter similar grid search, however, also shows convergence to a global minimum at α = -20° and t_{ref} = ~102% (Figure 5c). A vertical slice of the error surface at t_{ref} = ~102% shows that ε_{tot} converges to ~0 at α = -20°, the exact input value (Figure 5d). Although the data are devoid of errors, the use of an average perpendicular thickness value t_{ref} precludes ε_{tot} from obtaining a value of exactly zero. Clearly, the minimum similar solution is favored over the minimum parallel solution. In this synthetic example, then, the method easily differentiates between the correct (similar) and incorrect (parallel) solution while solving exactly for the input parameters.

Figure 6a is an example of a parallel fault bend fold resulting from LPS deformation with gently curving fold limbs digitized from an example by *Medwedeff and Suppe* [1997, Figure 12b]. We choose this example because its gently curving fold limbs more closely model many natural structures than angular forward models with planar limbs [e.g., *Suppe*, 1983]. In contrast to the AISS similar fold example, the grid search and misfit calculation for this example clearly favors a parallel solution. The parallel solution is strongly convergent and well constrained in Figure 6b and the misfit approaches zero. (Small digitizing errors in addition to the use of an average perpendicular thickness cause the nonzero misfit value in this case.) In comparison, the similar solution is not as strongly convergent and has misfit values greater than the parallel solutions (Figures 6c and 6d), though the solution does converge to a global minimum.

The previous examples show that the FSI method effectively favors and determines the correct parameters of synthetically generated fold layers when their geometry is known exactly, that is, when there is no experimental noise included in the data set. This is clearly a necessary condition for a method's validity; however, for it to be of real practical use in analyzing seismic reflection data, we must consider the effect that errors introduced by the seismic reflection method

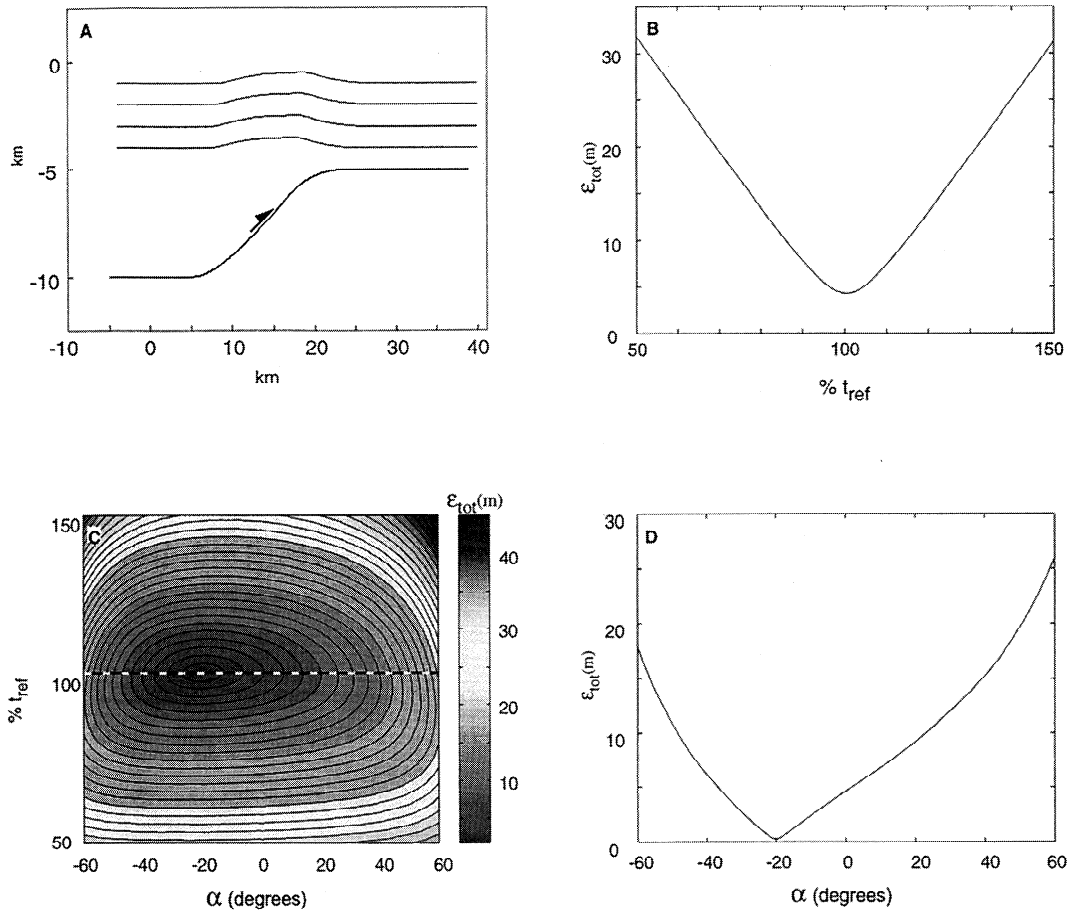

Figure 5. (a) Input suite of layers created by using AISS forward model and $\alpha = -20°$. (b) Results of parallel grid search. Horizontal axis is the parameter t_{ref}, and the vertical axis is the total error ε_{tot}. (c) Results of similar grid search. Horizontal axis is the parameter α, and the vertical axis is the parameter t_{ref}. Contours are on the total error ε_{tot} . Dashed white line indicates vertical slice at $t_{ref} = 1.02$. (d) Cross section of Figure 5c at $t_{ref} = 1.02$. Horizontal axis is the parameter α, and the vertical axis is the total error ε_{tot}.

have on the outcome of FSI analysis. Specifically, how do we know that a difference in ε_{tot} (Figures 5b, 5d and 6b, 6d) is significant?

3. Consideration of Errors and Application to Seismic Reflection Data

Because the FSI method operates on fundamentally geometric data, we apply it only to seismic reflection data that have been migrated and depth converted. Errors intrinsic to the acquisition, processing, and depth conversion of seismic reflection data are difficult to quantify because of the heterogeneous nature of the Earth itself, the subjective nature of processing, and the varying amounts of subsidiary information (such as well logs or synthetic seismograms) applied to any given depth conversion. Though it may not be possible to quantify precisely error at each step of the acquisition to depth conversion process, it is safe to assume that, for a seismic reflection line acquired and processed by using modern techniques, the most significant source of errors will be inadequate knowledge of a real-Earth velocity model used in depth conversion [*Al-Chalabi*, 1994].

Depth conversion errors are most likely due to unknown lateral velocity variations. These types of velocity anomalies may be present at any depth in a geologic section, and as such, they are independent of one another. However, the errors introduced when that same geologic section is imaged by using the seismic reflection method will be correlated between reflections at different depths. Clearly, seismic energy arriving at one reflective layer has passed through an Earth velocity field shared by all of the other reflective layers above it. Any travel time differences caused by a velocity anomaly at a certain depth will also be present in the travel times from all deeper reflections along the ray path (Figure 7a). Of course, lateral velocity variations present in deeper layers may also act to cancel out travel time errors produced by lateral velocity variations in shallower layers. If our grid search and misfit calculation is to be applied reliably to seismic reflection images of fault-related folds, we must take into account the velocity errors described above.

3.1. Monte Carlo Simulation of Depth Conversion Errors

To account for these potential errors and to derive confidence estimates on the preferred fold style solution, we integrate the FSI method with Monte Carlo simulations of a specific seismic reflection data set. Iterative Monte Carlo simulations and parameter estimations are a very effective means of determining confidence limits on parameters when error distributions are difficult to quantify for a specific data

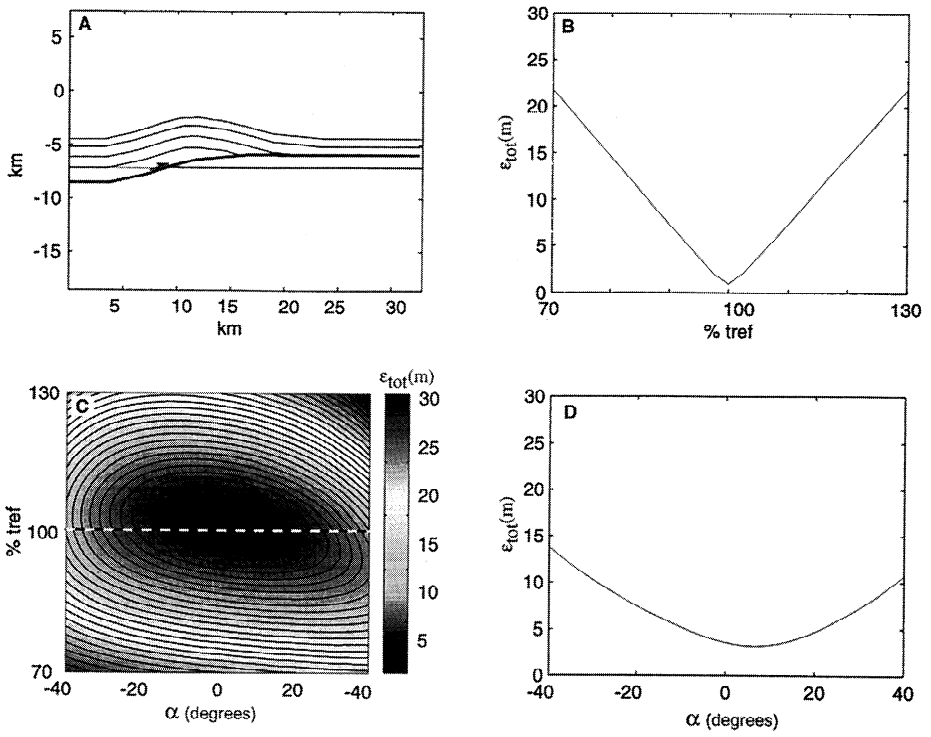

Figure 6. (a) Input suite of layers created using LPS forward model digitized from *Medwedeff and Suppe* [1997].(b, c, d) Results of parallel grid search, similar grid search, and vertical slice at $t_{ref} = 1$ as in Figure 5.

set though something about the error generation process is known [*Huber*, 1981; *Press et al.*, 1992]. In a manner analogous to the process developed by *Sandvol and Hearn* [1994] to estimate errors associated with seismic waveform inversion for shear wave splitting parameters, we perform iterative FSI inversions on data perturbed by a noise sequence which varies with each iteration. The noise sequence which we apply must have widths comparable to buried lithologic bodies and be correlative with depth.

We derive the noise sequence from reasonable amplitude and spatial distribution estimates of depth conversion errors caused by laterally varying velocity variations. Accordingly, in the same coordinate system as equation (1), we define a scalar-valued noise function specific to each layer, $e(x)$ as

$$e(x) = Aw(x_\lambda) \tag{5}$$

where A is a random amplitude (positive or negative) less than or equal to some maximum percent error and $w(x)$ is a white noise function sampled on x over some random wavelength greater than or equal to a reference wavelength λ but less than the length of the line (Figure 7b). The actual values of A and λ may be adjusted to the lithologic conditions specific to each seismic line. For example, if there is cause to believe that lithology is continuous over the length of the seismic line, then λ will be relatively large. Alternatively, A will be large and λ will be small if strong, short-wavelength, discontinuous lithologic variations exist in the geologic section. Because A is a percentage, when it is multiplied by bed depth (see below), the absolute magnitude of simulated errors will amplify with depth in a manner similar to actual seismic reflection depth conversion conditions. If we choose A conservatively, $e(x)$ represents a maximum error in depth conversion because it is independent of subsidiary information, such as well logs or synthetic seismograms, which serve only to improve depth conversion accuracy.

To apply this noise generation scheme to a given seismic line, we start by simply scaling each point in the shallowest digitized layer $\mathbf{a}_1(x)$ (in the notation of equations (1) and (2), with the subscript added to denote layer number) by equation (5):

$$\mathbf{a}'_1(x) = \mathbf{a}_1(x) + e_1(x)a_{\max}\mathbf{j} \tag{6}$$

where $a_{\max}$ is the maximum depth of a specific layer, $\mathbf{j}$ is a vertical unit vector, and $\mathbf{a}'_1(x)$ is the new reference layer to be used in FSI analysis (Figures 7c and 7d).

For deeper reflections we model correlative errors by the summation of errors specific to each reflection. Thus for all reflections,

$$\mathbf{a}'_i(x) = \mathbf{a}_i(x) + \left(\sum_{j=1}^{i} c_j(x)\right)a_{\max}\mathbf{j} \tag{7}$$

(Figures 7c and 7d). In FSI analysis the point wise transformations and misfit calculations (equations (1) and (2)) are all modified, then, by the substitution of $\mathbf{a}'_i(x)$ for $\mathbf{a}_i(x)$.

Independently of previous iterations, we repeat the application of equations (5) and (7) for a set of digitized layers. For each iteration the set of perturbed beds are then input to the grid search routine and a minimum misfit solution found for both the parallel and similar cases. In practice, we have found that 200 iterations is sufficient for convergence to a stable solution.

To illustrate the process, we show in Figure 8 the FSI results of 200 iterations for a purely geometric example of a

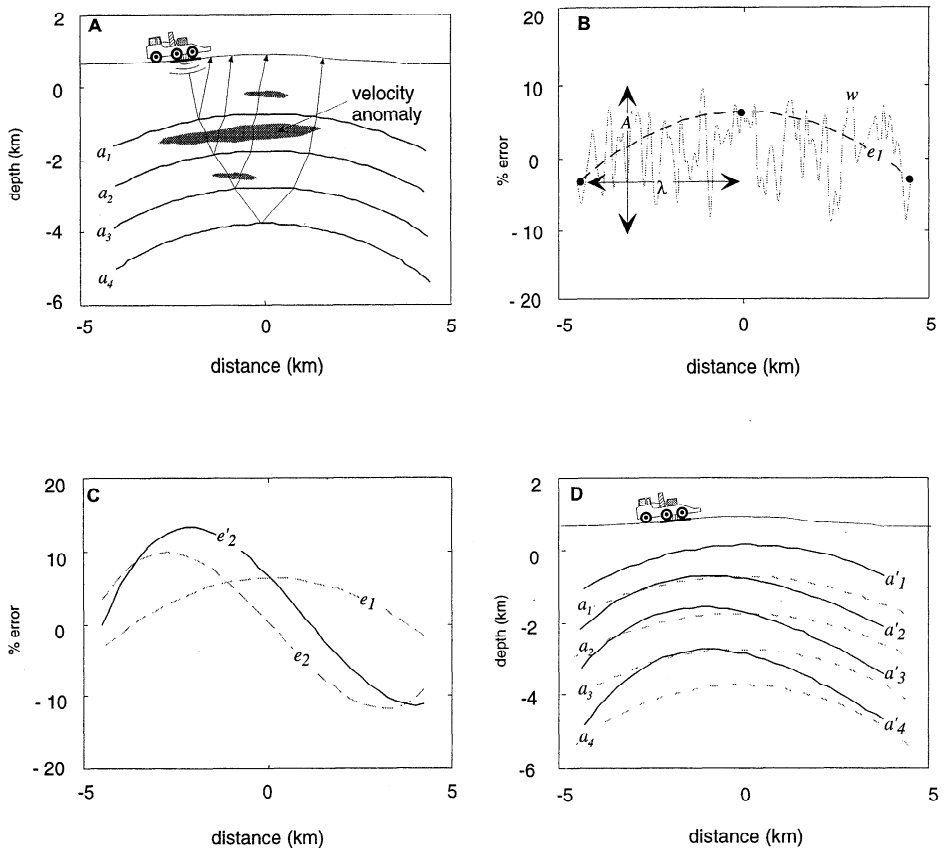

Figure 7. (a) Schematic diagram of seismic energy ray paths traveling through a folded, layered Earth with laterally varying velocity anomalies. (b) White noise function w (light dashed line) for the uppermost layer with a maximum amplitude A sampled over a minimum length λ to yield the error function, e_1(heavy dashed line) for the uppermost layer. Parameter w is independent for every bed and every iteration and is defined as a percent error in depth. (c) Summation of independent errors for the uppermost layer e_1 and the next lowest layer e_2, (dashed lines) to produce the correlated error e'_2 (solid line) for the lower layer. The summation of the independent error functions simulates ray-path-dependent velocity errors. (d) Error functions applied to the entire suite of layers (dashed lines) to produce the suite of layers for FSI analysis for one Monte Carlo simulation. The amplitudes of the errors (set by A in Figure 7b) is exaggerated greatly to demonstrate the simulations.

parallel fold. In this case we choose $A = 0.025$ and $\lambda = 3500$ m. Because we are trying to establish model preference, the minimum misfit ε_{tot} for each Monte Carlo realization (regardless of specific parameter values) of both the similar and parallel grid searches are plotted. In this example, the parallel solution is favored 100% of the time over the similar solution. From inspection we can see that the best solutions for each model never come within 2 standard deviations of each other's mean misfit value. Although the input model geometry is that of an exact parallel fold, the parallel grid search solutions never go to zero as in Figure 6b because of the introduction of the noise sequence in the Monte Carlo error simulations. Despite this error introduction, however, the method establishes a clear model preference. Clearly, we can degrade the data and the results of the grid search by adjusting A and λ, although the values we choose for the data in Figure 8 are typical of real seismic reflection data.

3.2. FSI Bias

Before we consider FSI application to realistic fold geometries, we investigate potential biasing of the results by introduction of the correlative noise sequence by applying FSI to entirely horizontal layers (Figure 9a). Straight layers oriented parallel to one another (of which horizontal layers are a subset) are examples of both similar and parallel folds as they satisfy simultaneously both equations (1) and (2). Because the layer geometry satisfies both the similar and parallel models, the misfit differences are much smaller than for the purely parallel geometry in Figure 8. If the error simulation process does not produce any bias, then we expect the differences in minimum misfit value $\Delta\varepsilon$ to fluctuate randomly about a mean value of 0. The similar grid search misfit values are consistently below, albeit a small amount, those for the parallel grid search (Figure 9a). We quantify this bias by plotting a discrete probability density function (DPDF) of the $\Delta\varepsilon$ values corresponding to each iteration where we define (Figure 9b)

$$\Delta\varepsilon = \varepsilon_{\text{similar}} - \varepsilon_{\text{parallel}}. \quad (8)$$

The field of the plot to the left of the origin indicates preference for the similar model, while the field to the right of the origin is the zone of parallel preference (Figure 9b). Clearly, the DPDF of the horizontal beds is slightly biased toward the similar zone; thus the application of the noise

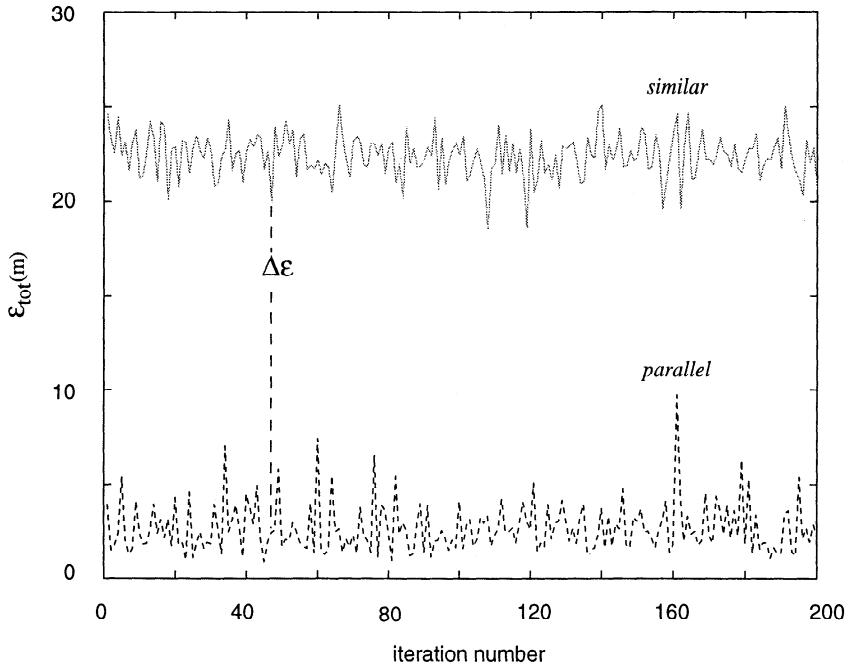

Figure 8. Plot of ε_{tot} versus iteration number for FSI analysis of concentric circles with a maximum limb dip of 45°. For each iteration the minimum misfit value for both the similar (solid line) and parallel (dashed line) grid searches are plotted. Concentric circles follow exactly parallel fold geometry, and the parallel solutions always have lower misfit values than the similar solutions. The parallel minimum misfit values do not reach zero because of the application of error in the Monte Carlo simulations. Here $\Delta\varepsilon$ is the difference of minimum misfit values defined in equation (8) as $\varepsilon_{similar} - \varepsilon_{parallel}$.

sequence introduces a bias toward similar folds in FSI analysis. The magnitude of this bias will vary with the magnitudes of the parameters A and λ in equation (5).

Quantifying the similar fold style bias is important when considering real data. Primarily, we must be able to demonstrate that a preferred solution (either similar or parallel) differs significantly from the slight bias imposed by the method. Below, using synthetic examples, we examine the factors which control solution differentiability.

3.3. FSI Resolution: Fold Limb Dip Dependence

We examine the FSI solutions for three synthetically generated parallel folds ranging in limb dip from 10° to 45° (Figures 10a, 10b, and 10c). The synthetic layers are simply arc lengths of concentric circles with different radii, a construction which satisfies the definition of parallel folding (equation (2)). For reference, we also plot the DPDF of $\Delta\varepsilon$ for the FSI results for horizontal layers at the same maximum depth as the data. We define the probability φ that $\Delta\varepsilon$ for an FSI iteration lies outside of the DPDF for the bias (horizontal beds) as

$$\varphi = 1 - \frac{\sum_{i=1}^{B} N_i}{I}, \tag{9}$$

where N_i is the lesser number of values for each $\Delta\varepsilon$ bin where there is overlap between bias and data, B is the total number of bins, and I is the total number of FSI iterations.

As maximum dip increases from 10° to 45°, φ increases from 0.54 to 1. The likeness of parallel and similar fold geometry at low dips is not surprising. The angular difference between a bedding normal vector at low bed dips and a vertically oriented vector is very small. In this case, equations (1) and (2) approach equivalence, and the distinction between parallel and similar fold geometry becomes insignificant.

This lack of differentiability between parallel and similar folds at low bed dips, strictly based on layer geometry, is significant to quantitative analyses of young active structures. Because the fault geometry resulting from the various fault solution methods may vary significantly [*Dula*, 1991], any uncertainty in folding style will carry over into predicted fault geometry.

4. Combining FSI and Fault Solution Routines

A flow chart illustrates the integration of the FSI method with the AISS and CBL fault solution methods (Figure 11). We stress that the algorithm may be entirely automated and is, essentially, an objective means of providing geometric solutions (specific to the chosen models) for blind faults. The most critical subjective choices are made during seismic reflection processing, the digitization of seismic reflections, and the assignment of the maximum error amplitude A and width λ in the error simulation process.

Processing (including migration and depth conversion) performed to industry standards will most likely be adequate to assure that processing errors are not the dominant source of error in final reflection geometry, though, obviously, examples must be evaluated on a case-by-case basis. Digitizing errors are also not likely to be a dominant error source, as they will generally have smaller magnitudes than the errors prescribed by the Monte Carlo simulations. Additionally, to prevent digitizing errors from becoming important, we choose for FSI analysis only those reflections

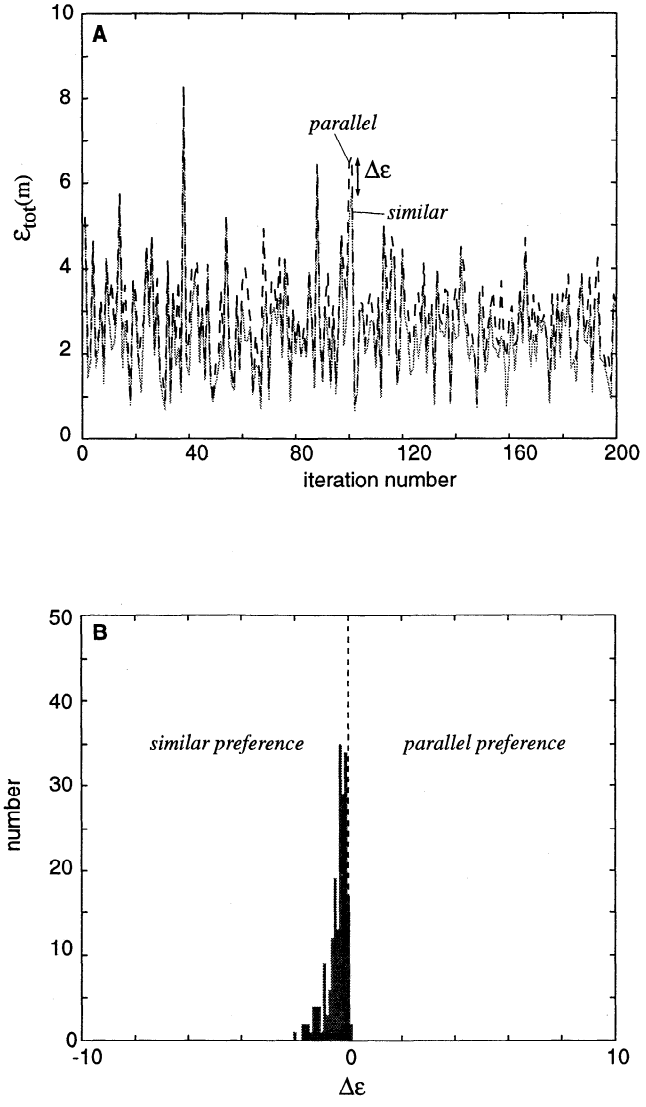

Figure 9. (a) Plot of ε_{tot} versus iteration number for FSI analysis of entirely horizontal beds. Although the $\Delta\varepsilon$ values are much smaller than those in Figure 8, the similar minimum misfit values are generally lower than parallel minimum misfit values. (b) Discrete probability density function (DPDF) of $\Delta\varepsilon$ for the data in Figure 9a. Negative $\Delta\varepsilon$ values indicate a preference for similar fold geometry, while positive $\Delta\varepsilon$ values indicate a preference for parallel folding. The DPDF for the horizontal layers lies almost entirely in the region of similar preference. This preference for similar folding is a bias imposed by the Monte Carlo simulation routine.

with clear continuity. Thus the largest potential source of subjectivity enters into the analysis through the choice of A and λ. Usually, standard velocity and stratigraphic data accompanying the seismic data are adequate to allow reasonable limits on λ and A to be made. Additionally, the multiple iterations of the error function allows random sampling of λ and A within these bounds (see discussion below).

We illustrate and test the entire method by analyzing a synthetic seismic reflection model of a fault bend fold (Figure 12). We use a standard ray-tracing package [*Yilmaz*, 1987] to model a 24-channel VIBROSEIS™ common midpoint seismic reflection survey over the model. The input layers have a similar fold geometry from an AISS forward model with α = -20°. The fault, with 5 km of slip, ramps from a lower décollement at 12 km to an upper detachment of 8 km over a width of ~15 km. The physical parameters of the model strata (p wave velocity, density, attenuation parameter, Young's modulus, etc.) are typical of those found in foreland fold and thrust belts [*Sheriff and Geldhart*, 1995]. We input the synthetic CMP shot gathers to standard processing software [*Yilmaz*, 1987] and perform semblance-enhanced velocity analysis to determine stacking velocities which we

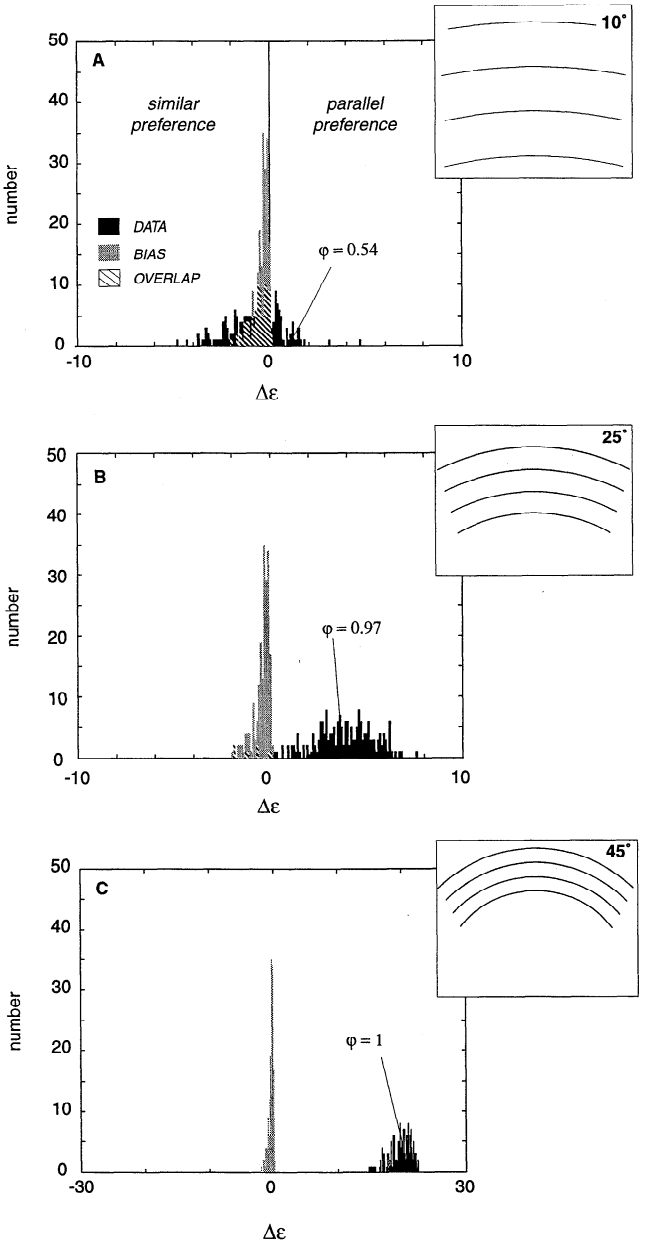

Figure 10. Three different sets of parallel layers plotted with the $\Delta\varepsilon$ DPDF for horizontal beds. The probability φ that a $\Delta\varepsilon$ value lies outside of the zone of overlap between the two distributions is defined in equation (9). (a) Maximum limb dips reach 10°. The diagonal lines indicate the zone of overlap between the $\Delta\varepsilon$ DPDFs for the horizontal layers and the data; φ = 0.54. (b) Maximum limb dips reach 25°. Diagonal lines as in Figure 10 a; φ = 0.97. (c) Maximum limb dips reach 45°. White diagonal lines as in Figure 10 a; φ = 1.

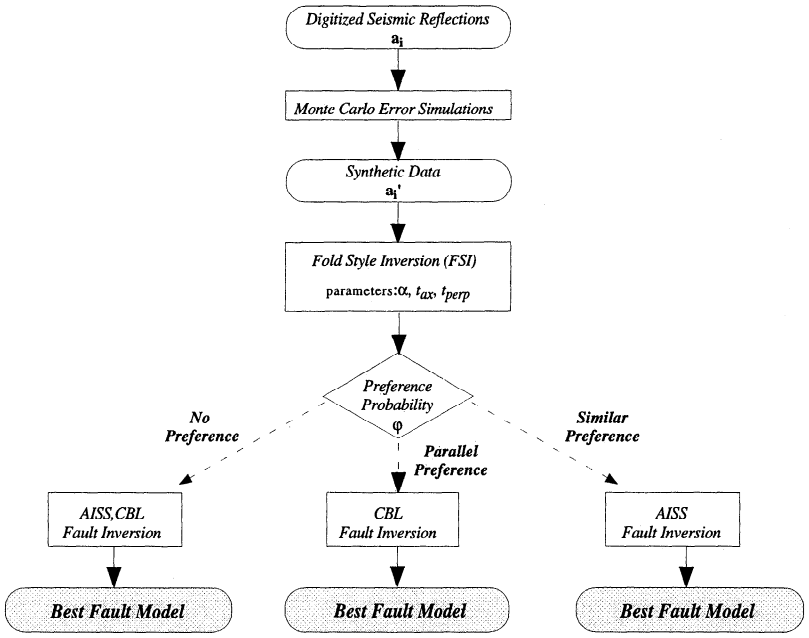

Figure 11. Flow chart demonstrating the FSI algorithm and the choice of the most appropriate fault inversion routine.

convert to interval velocities using the Dix equation [*Sheriff and Geldhart*, 1995]. Using these interval velocities, we migrate and depth-convert the data to produce the seismic reflection image (Figure 12a).

This processing flow is rudimentary; we do not perform seismic image-enhancing advanced processing techniques such as iterative velocity analysis combined with dip moveout application [*Deregowski*, 1986] nor depth migration [*Yilmaz*, 1987]. This simplistic processing is by design. We purposefully leave velocity errors in the data to see how these errors affect the final FSI analysis and fault inversion solution.

Because they record the entire fold shape, we digitize and perform FSI analysis on the uppermost four layers with A = 2.5% and λ = 8750 m (because our input velocity model does not contain any interlayer heterogeneities, we choose the λ value to be of the order of the wavelength of the fold). The FSI results show that over 200 iterations there is a 100% preference for a similar fold style with α = -20°± 10°(2σ) (Figures 12b and 12c). With these ranges of α and using the AISS fault inversion routine, we use the second-highest digitized bed to solve for the ranges of buried fault shape (Figure 12d). For comparison, we also show the CBL fault solution for the same bed (Figure 12d).

Both fault solutions are significantly different than the digitized reflection of the input fault. However, the AISS solution for the mean value, α = -20°, is essentially identical to the pre-seismic-shooting position of the model fault. The AISS solutions for the 2σ values, α = -10° and -30°, bracket the mean value solution with maximum differences of <~300 m. Because FSI analysis establishes a similar fold preference, this range of AISS solutions represents a 95% confidence interval for the predicted fault trajectory specific to the second-highest bed (assuming only two possible deformation mechanisms). In contrast, the CBL solution shallows to a décollement level ~2 km above the AISS solutions.

The discrepancy between the AISS solution and the fault plane reflection is caused by the increased velocity errors with depth leading to the downward shift of the fault plane reflection. In fact, by comparing input bedding geometry with depth-converted seismic reflections, we can track positional errors increasing down-section. The excellent agreement with the actual and AISS fault is because the bed used for the fault inversion is in essentially its correct position. Thus because fold geometry errors are small, the fault solution is a more accurate representation of the fault than the reflection of the fault itself.

This synthetic example is meant to illustrate solely that the seismic reflection method preserves fold geometry well enough for FSI to have discriminatory power given the combination of a large fold signal with relatively simple acquisition and processing. It should not be taken as general proof that the method will have discriminatory power with all seismic reflection data. We stress, however, that lack of FSI discriminatory power does not indicate that the method "fails"; rather, it is a quantitative indication that the data will not allow unique structural interpretations.

5. Application: Barrancas and Lunlunta-Carrizal Anticlines, Mendoza, Argentina

In this section we test the FSI method with seismic reflection data from the Barrancas/Lunlunta-Carrizal anticlinal complex situated at the eastern margin of the active Andean contractional deformation front in the Cuyo Basin at ~33°S, roughly 15 km south of Mendoza city, Argentina (Figure 13a). The region is located in the zone where the Precordillera thin-skinned fold and thrust belt loses surficial expression and is replaced to the south by the gentle anticlinal domes of the Cuyo fold belt (Figure 13a) [*Ramos et al.*, 1996]. The deformation front comprises east vergent blind thrust-related structures including fault propagation, fault

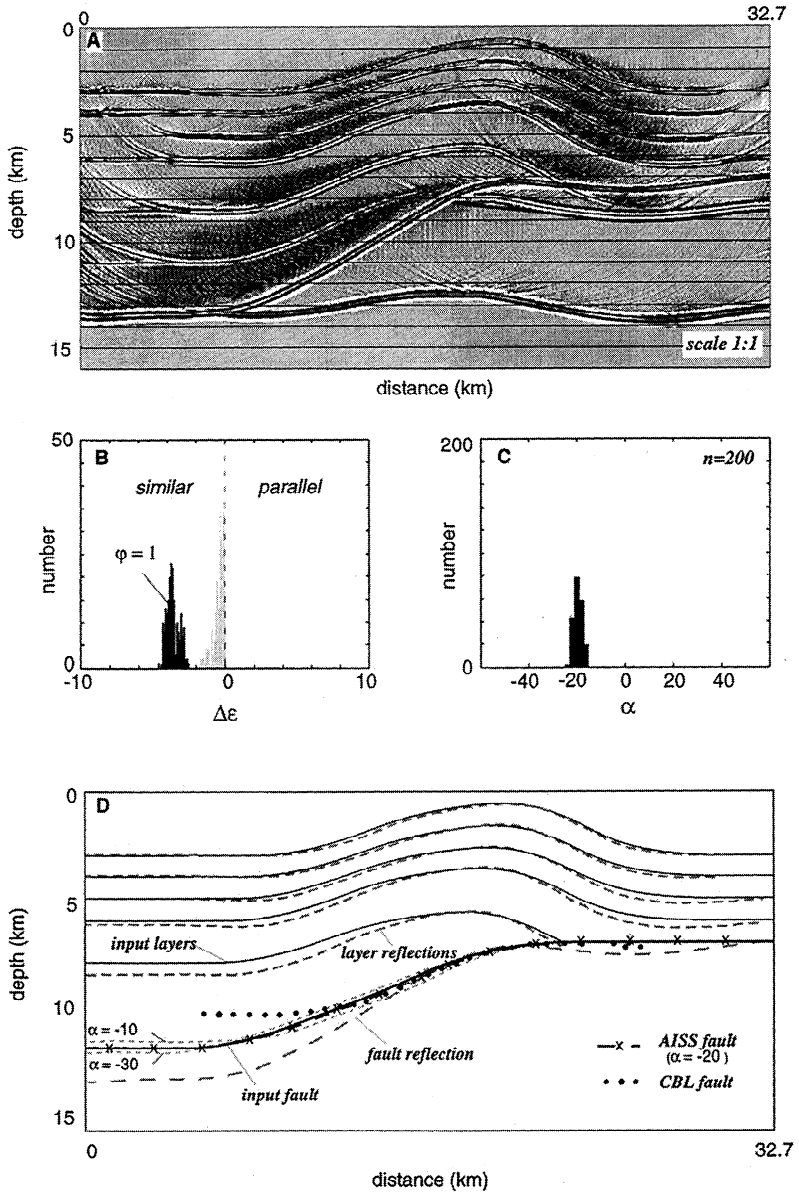

Figure 12. (a) Migrated depth-converted synthetic seismogram created for an AISS fault bend fold with α = -20°. (b) Plot of $\Delta\varepsilon$ DPDF for data (solid area) and horizontal beds (gray area); φ = 1, indicating a clear preference for similar fold geometry. (c) Histogram of the parameter α corresponding to each minimum misfit value of the data in Figure 12b with mean, -20°. (d) Cross section showing input beds (thin solid black lines), input fault (thick solid black line), digitized bed reflections (dashed lines), digitized fault reflection (dashed line), CBL fault solution (dotted line), and the AISS fault solution (dashed black line with crosses).

bend, and wedge folds [*Kozlowski et al.*, 1993; *Milana and Zambrano*, 1996; *Ramos et al.*, 1996; *Sarewitz*, 1988] associated with high levels of crustal seismicity (Figure 13a). In particular, the epicenter of the 1985 M_w 5.9 Mendoza earthquake is closely associated with the surface expression of the Barrancas/Lunlunta-Carrizal anticlinal complex (Figure 13b). The complex comprises two en echelon east verging anticlines extensively covered by YPF S.A. (Yacimientos Petrolíferas Fiscales Sociedad Anonima) seismic reflection profiles (Figure 13b). Some of the seismic reflection data image the top portion of a west dipping fault plane below the anticlinal complex (Figures 14a, 15b, and 17a). Paleozoic shelf strata of the Precordillera terrane [*Kokogian et al.*, 1993] comprise the faulted basement below ~1 km of Triassic continental syn-rift sediments which are overlain by ~3 km of foreland basin strata deposited in response to late Cenozoic Andean orogeny [*Irigoyen et al.*, 1999].

The relationship between Mendoza seismicity and the Barrancas/Lunlunta-Carrizal anticlinal complex remains unclear. Based on the asymmetry of the composite structure and its close proximity to the estimated epicenter of a ~M_s 7.1 earthquake in 1861, *Zamarbide and Castano* [1993] conclude that the west dipping fault below the anticlinal complex is responsible for the 1985 and 1861 earthquakes and the Neogene growth of the anticlinal complex. Both *Triep* [1987] and *Chiaramonte* [1996], however, on the basis of qualitative extrapolations of seismic reflection data and consideration of the published focal mechanisms and hypocenters (Table 1),

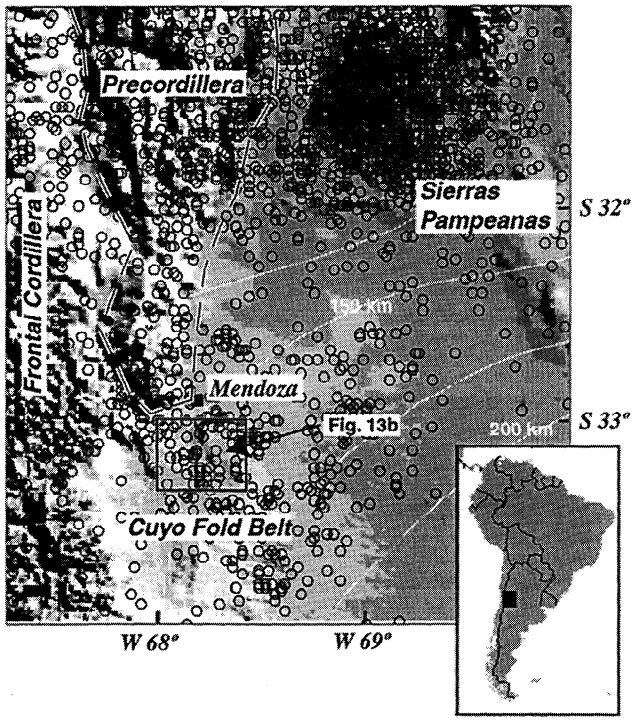
Precordillera
Frontal Cordillera
Sierras Pampeanas
S 32°
150 km
Mendoza
Fig. 13b
200 km
S 33°
Cuyo Fold Belt
W 68°
W 69°

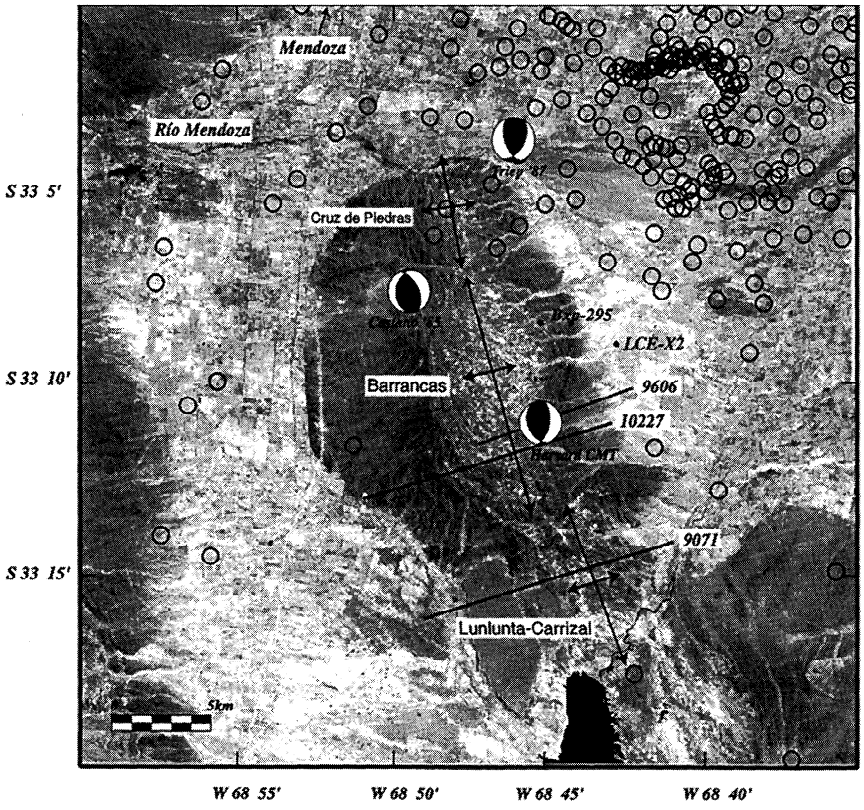
Mendoza
Río Mendoza
S 33 5'
Cruz de Piedras
Barrancas
S 33 10'
9606
10227
9071
S 33 15'
Lunlunta-Carrizal
5km
W 68 55'
W 68 50'
W 68 45'
W 68 40'

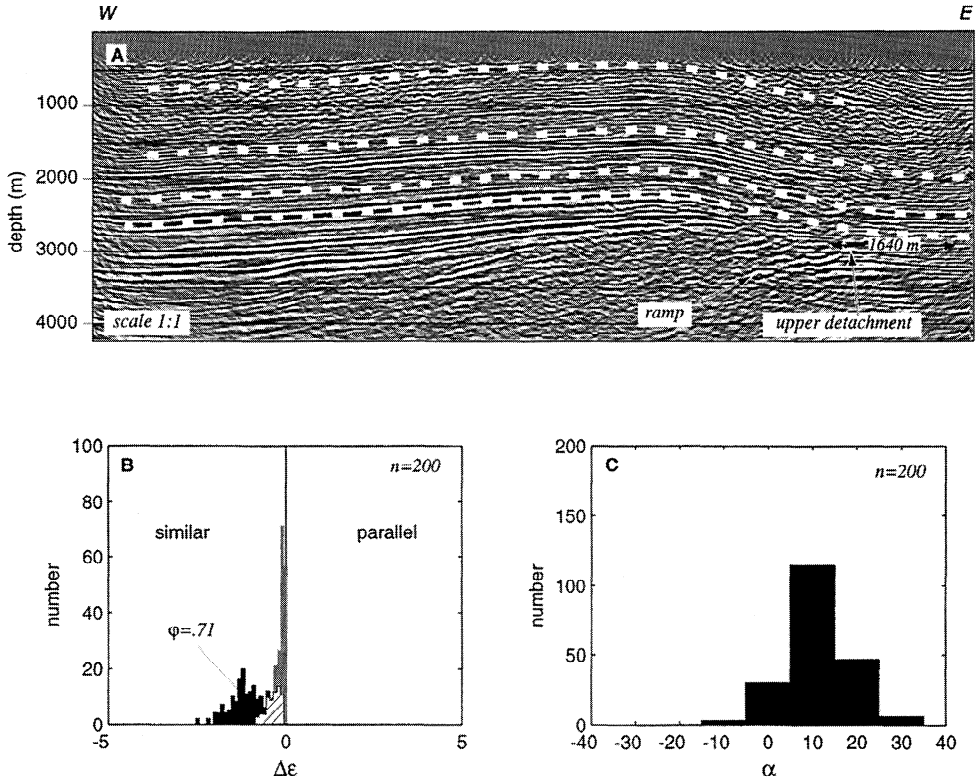

Figure 14. (a) Migrated depth-converted seismic reflection line 10227. The white dashed lines are the digitized reflections used in FSI analysis. Location of the fault ramp, upper detachment level, and measured slip are indicated. (b) Discrete probability density functions (DPDF) of $\Delta\varepsilon$ for the data (solid histogram) and horizontal beds (gray histogram) which represent the FSI bias toward similar fold style. The striped histogram is the area of overlap between the data and bias; φ is the probability that the data lie outside this zone of overlap. (c) Histogram of the parameter α from the FSI similar grid search.

support a model where a shallowly west dipping fault plane reaching a décollement level at ~7 km is responsible for fold growth, while a deeper west dipping plane was the seismic source in 1985. No quantitative examination of the subsurface fault geometry exists; thus FSI analysis can place fundamental quantitative constraints on the relationship between the anticlinal complex and the 1985 earthquake.

We analyze two dip lines (10227 and 9071, Figure 13b) in which hanging wall reflectors are well imaged, allowing us to measure fault slip for each line. Each of the lines are 120-channel 60-fold, VIBROSEIS™ lines. We migrated and depth-converted the lines by using an initial velocity model from a nearby sonic log (Figure 13b). On the basis of comparison with YPF synthetic seismic profiles and well logs and owing to the gentle nature of the fold limb dips, we estimate that vertical reflection accuracy is of the order of ±150 m. Only reflections which exhibit high degrees of coherence across an entire line are digitized and analyzed with FSI. Additionally, because we are trying to classify the bulk geometry of the strained hanging wall, we digitize beds over the widest range of depths possible.

In these seismic lines the Triassic syn-rift deposits are the highly reflective layers deeper than ~2500 m (Figures 14a, 15b, and 17a). These strata were deposited synchronously with extensional deformation; thus their geometry records hanging wall rotation due to Triassic normal faulting [*Kokogian et al.*, 1993]. Although they are continuous and well-defined reflectors, we do not include them in FSI analysis because their relict syn-rift layer geometry may distort any analysis, including post rift layers.

Figure 13. (a) Location map and regional physiographic map of the study area. Base map is a shaded relief 30 arcsec digital elevation model. The white contour lines are contours of the subducted Nazca plate from Wadati-Benioff zone earthquake hypocenters from *Cahill and Isacks*, 1992. The solid circles are earthquake epicenters of all crustal (< 60-km depth) events in the ISC catalog since 1964. The inset shows South America with the solid rectangle indicating the area of Figure 1a. (b) Land Sat Thematic Mapper gray scale image (bands 5,4,2) of the Barrancas and Lunlunta-Carrizal anticlines showing the limits of the Cruz de Piedras, Barrancas, and Lunlunta-Carrizal segments. Solid lines with numbers represent YPF S.A. (Yacimientos Petrolíferas Fiscales Sociedad Anonima) seismic reflection lines. Focal mechanisms of the 1985 M_w 5.9 Mendoza earthquake taken from *Triep* [1987], *Castano* [1995], and the on-line Harvard CMT catalog. The solid circles are epicentral locations of aftershocks from the 1985 Mendoza earthquake digitized from *Triep* [1987]. The solid dots are the positions of YPF boreholes with dipmeter (Bxp-295) and sonic log data (LCE-X2) used in this study.

Table 1. Parameters for the Focal Mechanisms of the 1985 M_w Mendoza Earthquake

Solution	Strike	Dip	Strike	Dip	Depth
Triep [1987]	160	56°W	030	46.9°E	14± 5
Castano [1995]	185	37°W	355	53°E	12
Harvard CMT	158	38°W	009	56°E	28.4± 1.7

5.1. Line 10227

Line 10227 images the asymmetric east vergent southern portion of the Barrancas anticlinal segment (Figure 14a). Fold geometry is reproduced very well, and fault plane reflections, though of poorer quality, are visible. In the eastern portion of the line, the high-amplitude Triassic syn-rift reflectors are duplicated, and an upper décollement level can be determined at ~3000 m depth. At the western limit of the upper décollement, a west dipping package of reflectors indicates the uppermost portion of the west dipping fault ramp. The interpretation of a fault bend fold with an upper décollement at ~3000 m is supported by dipmeter data from a borehole on the forelimb ~6 km to the north of line 10227 which records a sharp dip decrease at ~3000 m depth (Figure 15a). Additionally, line 9606 clearly shows Triassic hanging wall cut offs in contact with an upper décollement (Figure 15b).

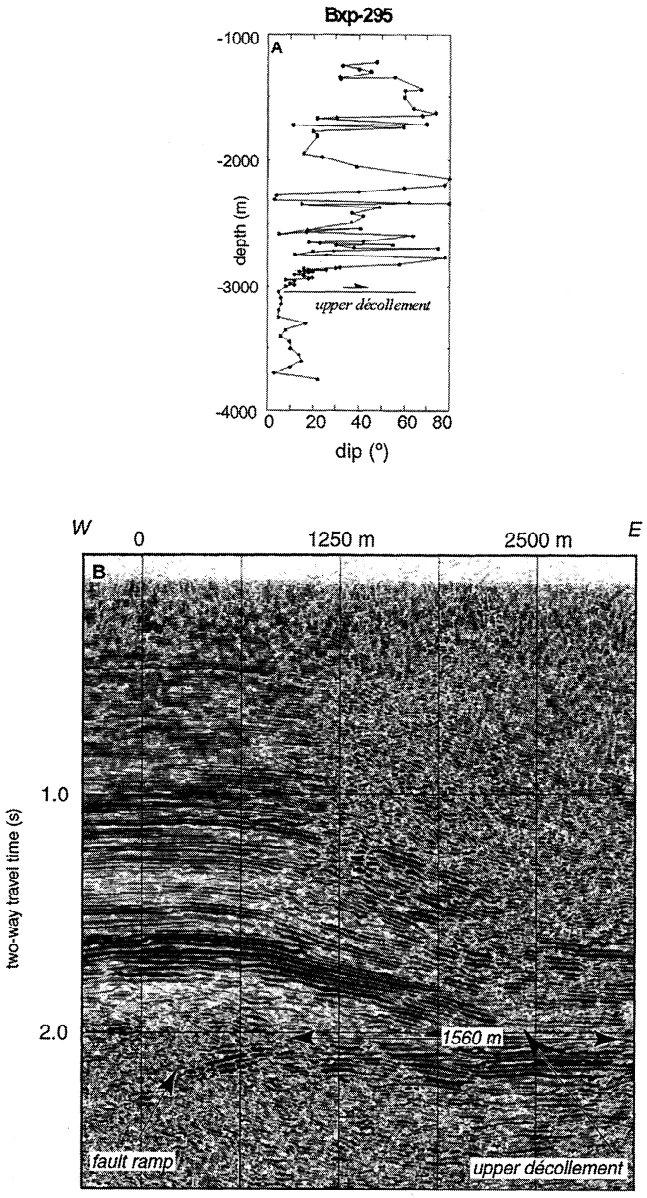

Figure 15. (a) Dipmeter data from borehole Bxp-295. All data dip toward the east. (b) Migrated time section of the eastern portion of seismic line 9606. Location of the fault ramp, upper detachment level, and measured slip are indicated.

We run the FSI routine for 200 iterations with maximum error amplitude, A = 2.5%, in accord with our estimation of ±150 m depth errors. Because the foreland basin stratigraphy is relatively continuous over the region, we assume that significant lateral velocity variations will be on a scale slightly smaller than the wavelength of the structure and we assign λ = 3 km.

The results, plotted as a discrete probability density function of $\Delta\varepsilon$ (Figure 14b), show that there is a 71% formal probability that a similar fold geometry may be separated from the slight FSI-imposed bias; thus there is a 71% formal probability that similar fold geometry is preferred over parallel fold geometry. The parameter α in the similar grid search is normally distributed with a mean value of 12° ± 14° (2σ) (Figure 14c). Thus an AISS model with inclined shear planes oriented 12° antithetically is the most likely of the models we consider. This result is consistent with two qualitative observations of fold style for line 10227: (1) the crestal position of each reflector moves from west to east as the reflectors get deeper and (2) back limb layer perpendicular thickness appears to be slightly greater than fore limb thicknesses.

Because the FSI method establishes a preference for similar fold style, the AISS fault inversion routine is preferred. FSI analysis provides the parameter α (Figure 14c), and so we only need to use one folded layer to find the fault shape (see the appendix). To test the consistency of our solutions, however, we solve for fault shape from the range of digitized beds. We only use the bottom three beds for fault inversion because the top most bed is truncated by an erosional surface, and so its synclinal hinge position, necessary for the AISS fault solution routine (appendix), cannot be accurately determined.

We estimate that there is 1640 m of slip on the upper detachment by projecting the structurally highest hanging wall cutoff down to the upper detachment; additionally, we estimate that this projection may be in error by as much as ±200 m. The preferred fault trajectories are found by using the mean value of α, 12°. The AISS fault trajectories are in good agreement and define a listric, concave-up fault surface which gently curves from a maximum west dip of ~25° near the upper portion of the ramp to a minimum dip of ~5° at ~

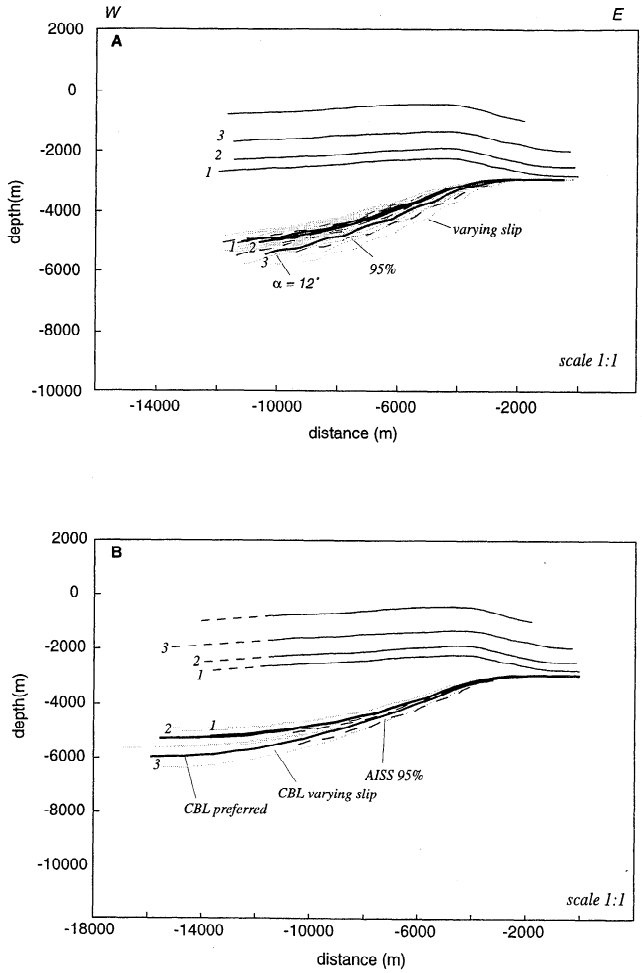

Figure 16. (a) AISS fault solutions for line 10227. The uppermost numbered solid lines are the digitized beds used in FSI analysis. The lowermost numbered solid lines are the preferred fault solutions found with $\alpha = 12°$ corresponding to the digitized beds with the same number. The dashed lines are the solutions for the $\pm 2\sigma$ α values (assuming only similar and parallel folding). The gray solid lines are the solutions if the measured slip is allowed to vary by ±200 m. (b) CBL fault solutions for line 10227. The dashed lines to the left of the digitized beds are the projection back to the regional level necessary for the CBL method to be valid. The solid lines are the preferred CBL solution. The gray solid lines are the solutions if slip varies by ±200 m. The dashed lines are the 95% AISS solutions.

6000 m (Figure 16a). Because the hanging wall layers do not extend the entire distance back to a regional level, the fault trajectories do not reach an exactly horizontal décollement level, although most likely the décollement level is between ~5500 and 6500 m for line 10227. Additionally, in Figure 16a we plot the range of solutions yielded when we take the 2σ range of estimated α and when we vary the slip on the upper detachment by ±200 m. The effect of varying α is small in comparison with the effect of varying the slip on the upper detachment. The depth range of solutions widens by ~± 300 m when the varying slip solutions are plotted.

For comparison, we show the CBL solutions with the same beds as the AISS solutions (Figure 15b). As is discussed in the appendix and by Geiser *et al.* [1988], to use the CBL method accurately, the hanging wall beds must reach the regional level. In Figure 16b we use the average dip of the backlimb layers to project the beds back to the regional level. The preferred CBL solutions, as well as the solutions when slip is varied by ±200 m, fall within roughly the same range of possible AISS solutions. Thus although it was not known a priori, in this example the different techniques do not yield very different fault solutions. Because the range of CBL fault solutions falls entirely within the 2σ range of AISS faults, we are able to conclude that the AISS range of faults represents the formal 95% confidence range for the solution routines considered by FSI. Had the CBL range of faults been outside of the AISS 2σ range, the formal confidence estimate on the AISS solutions would be at 68%, the product of 95% (2σ) and 71% (the FSI preference probability).

5.2. Line 9071

In Figures 17 and 18 we show the results of FSI analysis and subsequent fault solutions for line 9071 (Figure 17a) which cuts across the middle portion of the Lunlunta-Carrizal anticlinal segment (Figure 13b). Because lines 9071 and 10227 are ~7 km away from each other, we assume that stratigraphic character does not change and assign maximum error amplitude, $A = 2.5\%$ and $\lambda = 3000$ km. The results, plotted as a DPDF of $\Delta\varepsilon$ (Figure 17b), show that there is a 54% formal probability that a similar fold geometry may be separated from the FSI-imposed bias; thus there is a 54% formal probability that similar fold geometry is preferred over parallel fold geometry. The result that fold style is essentially indistinguishable does not come as a surprise, given that the fold limb dips in line 9071 seldom exceed 10°. As we saw in Figure 10, there is essentially no difference between parallel and similar fold geometry at limb dips of less than 10°. Thus because FSI analysis does not produce a clear preference, both the CBL and AISS solutions must be plotted and given equal weight.

We make similar seismic interpretations as for line 10227 and show the resulting family of fault solutions simply to illustrate the large variance when a structure has shallow limb dips (Figures 18a and 18b). Clearly, any further analysis based on one of these structural solutions will have a large value of difficult-to-quantify error associated with it.

We consider the FSI-constrained fault solutions together with main shock and aftershock hypocentral data [*Triep*, 1987] from the 1985 Mendoza earthquake (Figure 19). On line 10227 there is no overlap between any of the predicted fault trajectories and main shock or aftershock hypocenters projected onto a line striking 070° owing to the shallow nature of the fault solutions (Figure 19a). Additionally, the <20° fault dips are more than 20° shallower than the dips of the western dipping nodal planes for all of the focal mechanisms in Figure 13 and Table 1. It is highly unlikely, then, that slip on any of the fault solution planes could have produced the observed focal mechanisms. Line 9071 also shows very little coincidence of earthquake hypocenters and fault solutions, though the deepest fault trajectories, a small number of westernmost main shock hypocenters, and the INPRES main shock hypocenter overlap (Figure 19b).

Consideration of the map view pattern of the aftershock data in conjunction with the cross-section data supports the interpretation that it is highly unlikely that there is any connection between the faults beneath the Barrancas and Lunlunta-Carrizal anticlines and the 1985 Mendoza

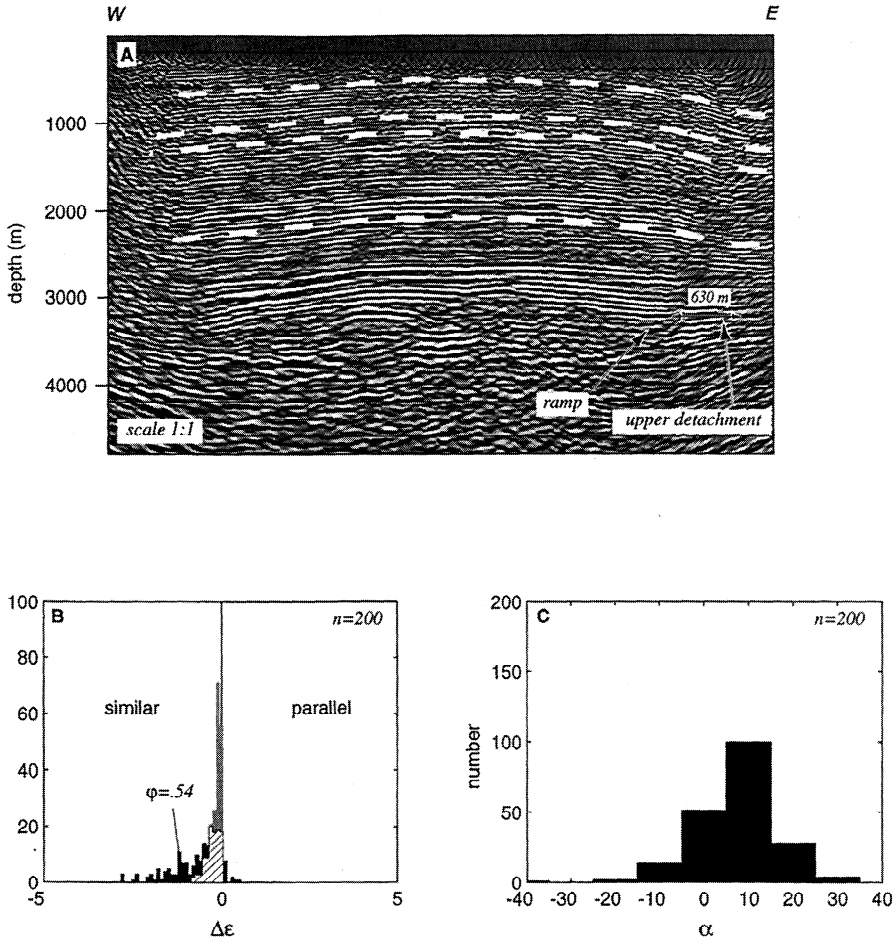

Figure 17. (a) Migrated depth-converted seismic reflection line 9071. The white dashed lines are the digitized reflections used in FSI analysis. Location of the fault ramp, upper detachment level, and measured slip are indicated. (b) DPDFs of $\Delta\varepsilon$ for the data (solid histogram) and horizontal beds (gray histogram). The striped histogram is the area of overlap between the data and bias; φ is the probability that the data lie outside this zone of overlap. (c) Histogram of the parameter α from the FSI similar grid search.

earthquake. Another possible explanation may be that, as with many blind-thrust-related earthquakes [*Stein and Yeats*, 1989], the aftershocks of the 1985 Mendoza earthquake occurred in the hanging wall of a reverse fault. Given the existing main shock and aftershock locations, this would imply that the earthquake occurred on an east dipping plane below the zone of aftershocks. Without further earthquake studies, however, this interpretation remains solely a viable hypothesis.

6. Discussion

The FSI method developed in this paper provides an objective basis for choosing between similar and parallel fold styles and for placing confidence limits on the predicted subsurface fault trajectories of blind thrust faults. To the best of our knowledge, placing subsurface fault trajectories in such a probabilistic framework has not been practiced previously in the analysis of fault-related folds, although high enough quality seismic reflection data often exist to do so. We suggest that if an FSI-like treatment is not undertaken, blind thrust analyses may be significantly underrepresenting the nonuniqueness associated with subsurface fault prediction and, accordingly, the uncertainty in the presented interpretation.

For instance, in their important paper, *Shaw and Shearer* [1999] use a fault-related fold model to link fault plane seismic reflections below the Santa Fe Springs anticline with the relocated hypocenter and focal mechanism of the 1987 *M* 6.0 Whittier Narrows earthquake beneath metropolitan Los Angeles. Establishing such connections between surficial fold features, fault plane reflections, and earthquake sources is crucial if paleoseismologic-like analyses of blind thrusts are to be developed. However, no discussion is given by *Shaw and Shearer* [1999] of alternative fault-related fold models, nor of errors associated with extrapolating a fault-related fold model over ~12 km distance. As we see in both the synthetic and field examples in this paper, errors due solely to uncertainty in fold style can be significant. In our best example, the preferred fault solutions for line 10227 (assuming that our measured slip value is correct) have ~ 1km downdip depth differences, while the 95% confidence limit range of solutions has slightly larger differences. Such errors applied to integrated structural and seismologic analyses will make earthquake/fault/fold connections such as those of *Shaw and Shearer* [1999] less certain. Alternatively, if it can be

shown that fault-related fold model errors are smaller, the final interpretation is strengthened.

It is important to realize that FSI's confidence limits are only formal confidence limits which describe the probability of preference between two ideal fold styles assuming that depth conversion errors, and our simulation of them, are the sole error source in a final seismic reflection image. These fold style errors, however, are only one contribution along with myriad other error sources which complicate quantifying the actual error of a particular seismic reflection image and model-based analysis of a fault-related fold. For instance, other significant error sources may be poor seismic acquisition and imaging, heterogeneous deformation mechanisms, and inaccurate slip determination. As we saw in the examples from the Barrancas/Lunlunta-Carrizal anticlinal complex (Figures 16 and 18), uncertainty in measured slip can dominate the uncertainty in predicted fault trajectories. This is, however, a source of uncertainty which will always be present in analyses of seismic reflection data and is only remedied by higher-quality data. In contrast, FSI addresses uncertainty in the modeling process (the assignment of fold style and choice of a fault solution routine) which is fundamental in blind thrust analyses yet sensitive to subjective biases.

In this paper we have shown explicitly (Figure 10) that fold style resolution decreases with decreasing fold limb dip. This effect is most important for analyses of the youngest (and presumably most active) structures which have not been active long enough for limbs to achieve dips greater than 10°. Furthermore, the ability of the FSI method to choose the correct fold style in the synthetic seismic example (Figure 12) shows that the seismic reflection method can reproduce fold geometry well enough so that FSI analysis is valid. Thus before a fault solution method is chosen, a method such as FSI should be undertaken to determine if fold style is distinguishable. If fold style is distinguishable, then the preferred fault solution method may be used with a formal probability estimate taken from equation (9) (assuming that there are only two possible fold styles); if fold style is not distinguishable, then all fault solutions must be reported in order to represent fairly the range of possible solutions. The range of possible solutions should then be carried over into any analysis such as calculations of fault ramp area, shortening rate, and/or earthquake recurrence interval. The analysis of line 9071 from the Lunlunta-Carrizal anticlinal segment (Figure 18) is an example of how fault solutions associated with young gently dipping structures may have large degrees of structural uncertainty associated with them.

At this point in the development of FSI we only consider parallel (class 1B) and similar (class 2) fold styles because they are associated with the deformation mechanisms assumed by the CBL and AISS methods, respectively, the two most widely used fault solution routines. To the best of our knowledge, however, fault solution routines associated with the other dip isogon classes (1a,1c, and 3) do not currently exist, though other well-documented folding mechanisms such as buckling or trishear will produce nonparallel and nonsimilar folds. Thus although the dip isogon classification is general and FSI may be modified fairly simply to include the other fold classes, carrying the probability estimates through to subsurface fault trajectories is dependent on the

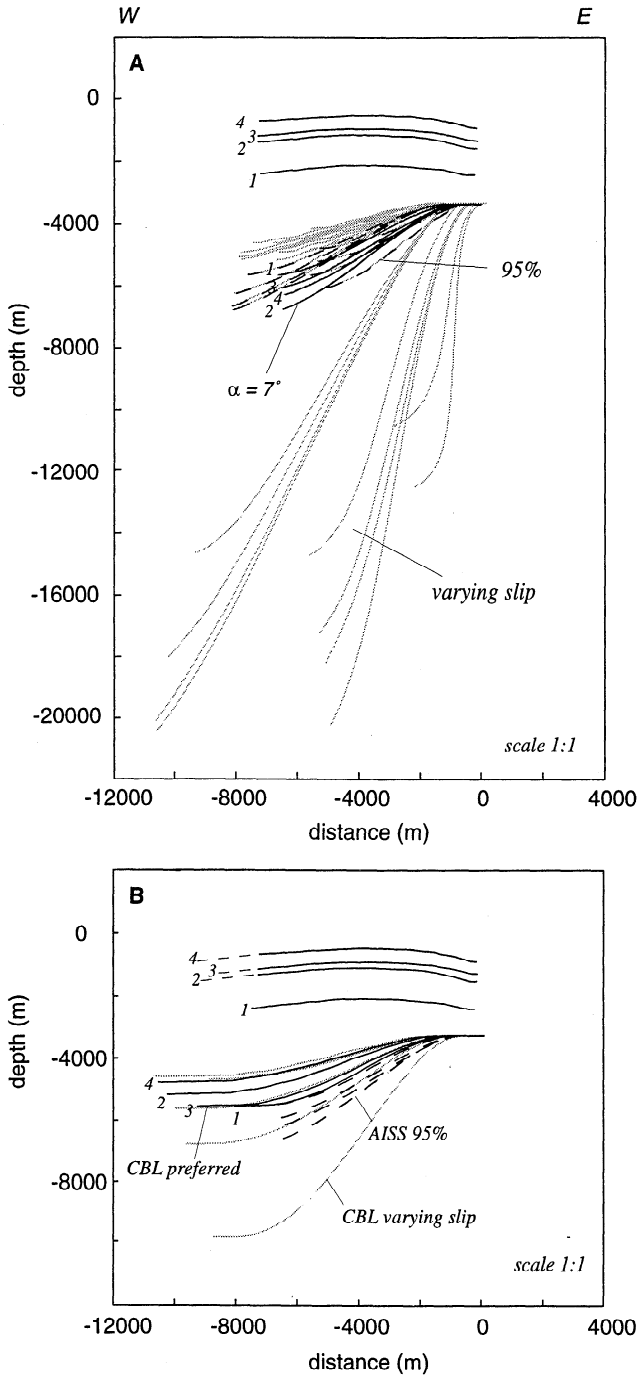

Figure 18. (a) AISS fault solutions for line 9071. The uppermost numbered solid lines are the digitized beds used in FSI analysis. The lowermost numbered solid lines are the preferred fault solutions found with $\alpha = 7°$ corresponding to the digitized beds with the same number. The dashed lines are the solutions for the $\pm 2\sigma$ α values. The gray solid lines are the solutions if the measured slip is allowed to vary by ±200 m. (b) CBL fault solutions for line 9071. The dashed lines to the left of the digitized beds are the projection back to the regional level necessary for the CBL method to be valid. The solid lines are the preferred CBL solution. The gray solid lines are the solutions if slip varies by ±200 m. The dashed lines are the preferred AISS solutions.

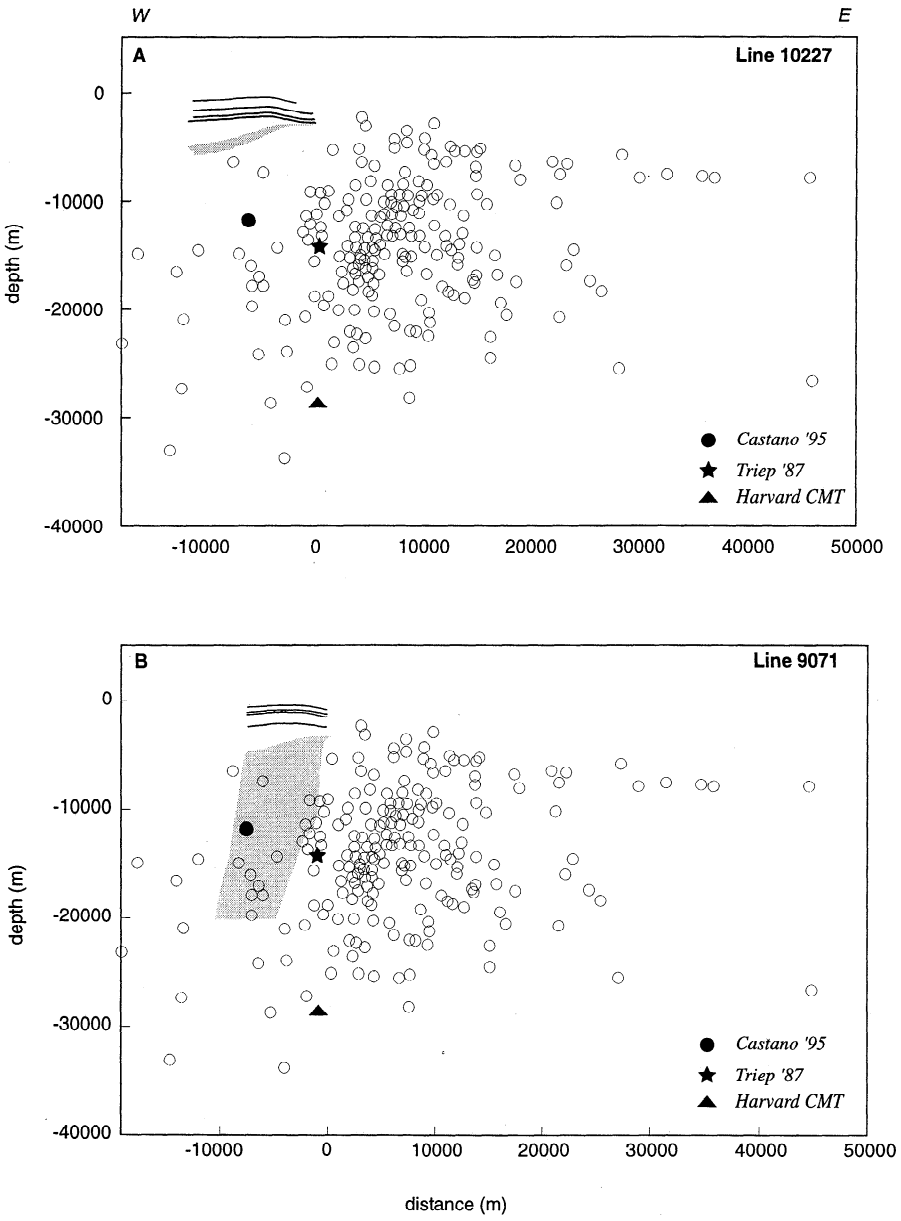

Figure 19. (a) Digitized beds and the entire range of fault solutions for line 10227 plotted with hypocentral locations of earthquakes related to the 1985 M_w 5.9 Mendoza earthquake. The solid symbols indicate hypocentral locations of the main shock from *Triep* [1987], *Castano* [1995], and the on-line Harvard CMT catalog. Open circles indicate aftershock hypocentral locations projected onto a plane striking 070° from *Triep*, 1987. (b) Digitized beds and the entire range of fault solutions for line 9071 plotted with the same earthquake data as Figure 19a.

development of corresponding fault solution routines. Regardless, more robust results are always obtained by testing most models, and future development of FSI will include the other dip isogon fold classes.

Additionally, in its current formulation FSI does not explicitly address nonhomogeneous deformation mechanisms nor fold geometry produced when growth stratal layers are included. It does, however, provide a quantitative basis for assessing the simple fold styles. If poor differentiability between models cannot be attributed only to low fold limb dips, then it is likely that the deformation mechanism is more complicated than the simple ones tested with FSI or that growth stratal layers have been included in the analysis. If the interlayer geometrical relationship between points for some nonhomogeneous deformational style or growth stratal configuration may be described by one of the other dip isogon fold classes or may be specified mathematically, then FSI's misfit calculation and Monte Carlo error simulation routines may be applied.

It is important to consider how the choice of the parameters, A and λ, affect the overall Monte Carlo simulation of depth errors. Conservative bounds on A, the error amplitude, are fairly straightforward to estimate for a given data set. Typically, the accuracy of a final seismic reflection image may be estimated from borehole or synthetic sections associated with industry seismic lines allowing a direct estimate of A; λ estimates are slightly more difficult, though reasonable bounds may be placed on them. Our tests

show that if λ is small in relation to the fold limb width, then the net error produced is essentially a random noise about the reflection. This random error will not contribute to a fundamental change of shape; thus small-wavelength error is negligible. If λ is much larger than the fold limb length, then the effect is a constant vertical shift of the layer, without a change of shape. These types of velocity anomalies on the scale of the entire structure are also more likely to be detected and corrected for by standard methods. Thus it is the λ variation over an intermediate-scale range which can have the most important effect on FSI analysis. In the iterative error simulations we explicitly account for this variation by randomly varying λ between the two bounds. Thus because the upper bound on λ is fixed automatically (the length of the line), the choice of a lower bound on λ is the most subjective aspect of FSI. If standard regional stratigraphic data exist for a region, however, then it is most likely that a good lower estimate of λ may be made.

Regionally, FSI analysis gives quantitative basis to the interpretation that the fault coring the Barrancas/Lunlunta-Carrizal anticlinal complex is not related to the 1985 Mendoza earthquake and aftershock sequence. This is particularly important given that the structure lies ~15 km to the south of one of Argentina's more densely populated and important cities, and determining both the source of the 1985 earthquake and the seismic potential of the Barrancas/Lunlunta-Carrizal anticlinal complex has been an unresolved issue. Instead of one preferred fault solution, we present a family of possible solutions with corresponding formal confidence limits. We stress, however, that our confidence limits are based on only two of myriad deformational mechanisms; thus while FSI-based analysis is more rigorous than previous studies, clearly more can be done to further quantify the structural solution at the Barrancas/Lunlunta-Carrizal anticlinal complex.

7. Conclusions

1. We have introduced the fold style inversion method as an objective tool to assess the goodness of fit of specific fold styles by using the dip isogon classification scheme. Objective fold classification allows an objective choice of methods used in solving for the depth profile of a fault from overlying fold geometry. In FSI, we employ Monte Carlo simulations of folded layer geometrical errors to mimic depth conversion errors in seismic reflection data. This approach allows formal confidence limits to be placed on fold style and, subsequently, on the predicted trajectory of a blind fault. Although the method is general, in our development we only consider parallel and similar fold styles because of their correspondence with the widely used CBL and AISS fault solution methodologies.

2. We have shown explicitly that for parallel and similar folds with gentle limb dips (<~15°) fold style becomes indiscriminate. This has important ramifications for seismic hazard analyses of young structures whose fold limbs are still shallowly dipping.

3. The FSI method works exactly on synthetic geometric data sets and on a synthetic seismic section meant to replicate modern exploration surveys. The synthetic seismic example suggests that, for fold geometries where seismic imaging is good, the seismic reflection method can adequately reproduce fold geometry so that it can be distinguished quantitatively by FSI.

4. To illustrate the method, we have placed quantitative constraint on the relationship between the Barrancas/Lunlunta-Carrizal anticlinal complex and the M_w 5.9 1985 Mendoza, Argentina, earthquake. Considering only parallel and similar folding, we have mapped the fault below the anticlinal complex in a zone of 95% confidence and shown that it is highly improbable that the earthquake and its aftershocks are associated with the fault.

Appendix

AISS Deformation and Fault Inversion

AISS forward and inverse fault-related fold modeling has been used almost exclusively in extensional terranes [e.g., *Kerr and White*, 1996]; here we describe the method for use with contractional structures using the same terminology from *White et al.* [1986]. Generally, during AISS deformation, area is conserved, the fault does not change shape, and no gaps or overlaps between the hanging wall and the fault surface are allowed to form. During fault slip, hanging wall material points are translated horizontally and then sheared upward along planes which deviate from the vertical by the angle of inclined simple shear, α [*White et al.*, 1986]. Fault heave h is conserved in some reference frame rotated by α [*White et al.*, 1986] (Figure A1a). If $\alpha = 0$, then the coordinate system in which h is conserved has horizontal and vertical axes. The coordinate system in which h is conserved is rotated clockwise by α if $\alpha < 0$ and counterclockwise if $\alpha > 0$.

In the forward problem, in the coordinate system rotated by α (signified by primed variables), the vertical distance between each material point, $R'(x')$, on a regional level and the fault, $F'(x')$, is equal to the vertical distance between a

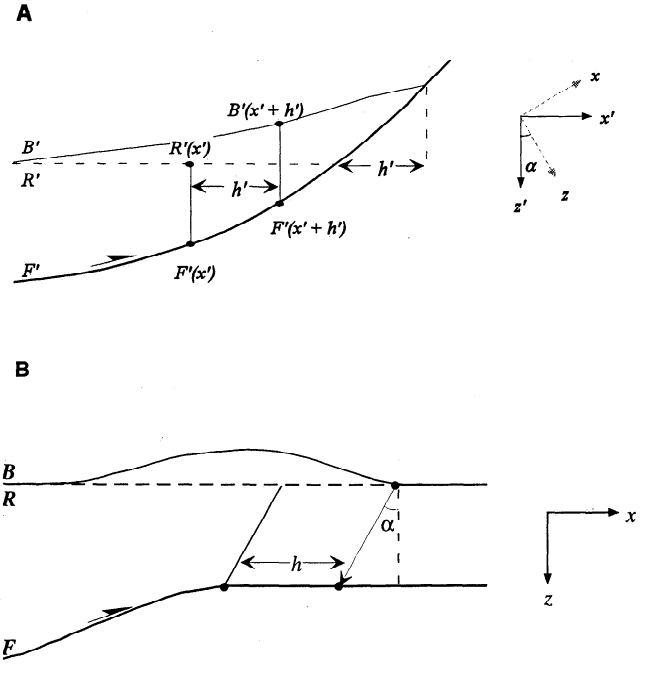

Figure A1. (a) General AISS thrust fault deformation in the coordinate system, rotated by α, used to derive equation (A1) after *White et al.* [1986]. $F'(x')$ and $F'(x'+h')$ are points on the fault, $R'(x')$ is a point on the regional level, $B'(x'+h')$ is a point on the deformed bed, and h' is the fault heave. (b) AISS fault bend fold adaptation.

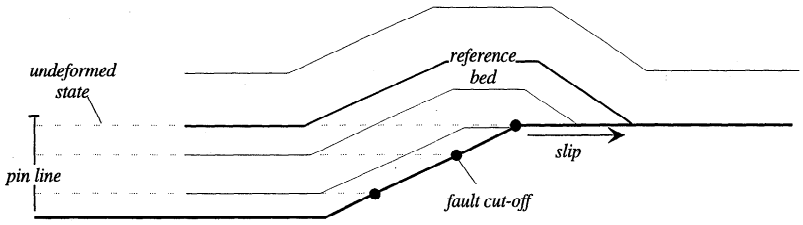

Figure A2. CBL fault inversion routine after *Geiser et al.* [1988]. The first bed is found by projecting the position of the synclinal hinge down to the upper detachment along the hinge line. The length of the reference bed is restored to a horizontal position to find a regional pin line. Lower beds are found by using a parallel projection (equation (2)). The bed lengths are restored to the regional pin line, and the restored cutoff positions define the position of the fault plane.

point displaced a distance h' from $R'(x')$, $B'(x'+h')$, and the fault, $F'(x'+h')$ (Figure A1a). This is described simply by equation (2) from *White et al.* [1986]:

$$R'(x') - F'(x') = B'(x'+h') - F'(x'+h'). \qquad \text{(A1)}$$

In the inverse problem, if the fault surface is known over a minimum distance of h', then $R'(x')$, $B'(x'+h')$, and $F'(x'+h')$ are known and $F'(x')$ is found by rearranging equation (A1). The remaining points on the unknown fault surface are solved sequentially from structurally higher to lower positions. Once the bed reference points ($B'(x'+h')$) are more than a distance h' from the initial starting point, then the fault reference points ($F'(x'+h')$) will be points solved for in prior steps.

In their formulation of the problem, *White et al.* [1986] and *Kerr and White* [1996] invert simultaneously for the shape of the fault as well as for α; thus because there are more than one unknown variables, it is required that more than one digitized bed be used in the fault solution. However, if α is known, then the shape of the fault may be calculated directly from the shape of the bed using equation (A1). In our implementation, because FSI directly estimates α, we may calculate fault shape from the shape of only one digitized bed.

Layer Parallel Slip and CBL Fault Inversion

Parallel fault-related folds form when beds maintain layer thickness and length as hanging wall material, deforming by layer parallel slip LPS, slips past bends on underlying faults [*Suppe*, 1983]. As with the AISS model, area is conserved, the fault does not change shape, and no gaps or overlaps between the hanging wall and the fault surface are allowed to form during deformation. Ignoring secondary effects such as homogenous shear imposed over the hanging wall [*Mosar and Suppe*, 1992], LPS fault bend fold geometry is uniquely determined by fault shape through simple trigonometric relations described by *Suppe* [1983].

The CBL method has been used to solve for thrust fault geometry given deformed hanging wall beds, and we refer the reader to *Geiser et al.* [1988] for a thorough explanation of the method. In order to adapt the CBL method to fault bend folds, the shape of the layer which shares a regional level with the level of the upper décollement must be known. If this reference layer is not directly imaged, then it may be found by projecting the shape of a structurally higher layer to the upper décollement level by using a parallel fold projection (equation (2)). The reference layer is restored to an undeformed orientation and a regional pinline is chosen (Figure A2). In the deformed state, bed shapes must be known at least to the point where they intersect the regional level, or pinline position will be incorrect. Again using the parallel fold projection, the layer below the reference layer is calculated. The projection length must be small enough that the hanging wall cutoff of the calculated bed occurs where there is information about fault shape. The calculated bed is then restored to the previously defined regional pinline and the restored position of the hanging wall cutoff is the fault position at a vertical depth equal to the regional level of the restored bed. In this way, the entire shape of the fault is solved for iteratively from structurally higher to lower positions (Figure A2). As the solution algorithm progresses, the restored-state hanging wall cutoffs will be found with respect to fault points which are unimaged but have been solved for in prior steps.

Acknowledgments. We thank Rick Allmendinger, Terry Jordan, Francisco Gomez, Alex Calvert, and Elias Gomez of Cornell University for many helpful discussions, fruitful suggestions, and reviews of this paper. This work would not have been possible without the generosity of YPF S.A., who provided us with seismic reflection data, well data, and assistance in the field. We especially thank Rene Manceda of YPF S.A. for his encouragement and numerous discussions. We thank Roberto Villa, Juan Scolari, Miguel Marnetti, and Marta Bugarini of YPF S.A. in Mendoza for assistance with seismic data and field support. We thank also Tomas Zapata of YPF S.A. in Neuquen for discussions and joint field work. We thank the National Science Foundation for supporting this research under grant EAR-9614759. Finally, we thank JGR reviewers Donald Medwedeff, Thomas Brocher, and Yosio Nakamura for particularly careful reviews and helpful suggestions which greatly improved the clarity of this paper. SOEST contribution no. 5167.

References

Al-Chalabi, M., Seismic velocities - A critique, *First Break*, *12* (12), 589-596, 1994.

Cahill, T., and B.L. Isacks, Seismicity and shape of the subducted Nazca plate, *J. Geophys. Res.*, *97* (B12), 17503-17529, 1992.

Castano, J.C., *Microzonificatión Sismica del Gran Mendoza*, 156 pp, Inst. Nac. de Prevención Sísmica, Mendoza, Argentina, 1995.

Chiaramonte, L., Estructura y sismotectonica del anticlinal Barrancas (Provincia de Mendoza), trabajo final de licenciatura thesis, Univ. de Buenos Aires, Buenos Aires, 1996.

Deregowski, S.M., What is DMO?, *First Break*, *4* (7), 7-24, 1986.

Dula, W.F., Geometric models of listric normal faults and rollover folds, *Am. Assoc. Pet. Geol. Bull.*, *75* (10), 1609-1625, 1991.

Elliot, D., The quantitative mapping of directional minor structures, *J. Geol.*, *73*, 865-880, 1965.

Erslev, E.A., Trishear fault-propagation folding, *Geology*, *24*, 617-620, 1991.

Geiser, J., P.A. Geiser, R. Kligfield, R. Ratliff, and M. Rowan, New applications of computer-based section construction: strain

analysis, local balancing, and subsurface fault prediction, *Mt. Geol.*, *25*, 47-59, 1988.

Huber, P.J., *Robust Statistics*, 308 pp., John Wiley, New York, 1981.

Hudleston, P.J., Fold morphology and some geometrical implications of theories of fold development, *Tectonophysics*, *16*, 1-46, 1973.

Irigoyen, M.V., and M.E. Villeneuve, Calibration of a Neogene magnetostratigraphy by ^{40}Ar-^{39}Ar geochronology: The foreland-basin strata of northern Mendoza, Argentina, in *Radiogenic Age and Isotopic Studies, Rep. 12*, pp 27-41, Geol. Surv. Can., Ottawa, Ont., 1999.

Kerr, H.G., and N. White, Kinematic modelling of normal fault geometries using inverse theory, in *Modern Developments in Structural Interpretation, Validation and Modelling*, edited by P.G. Buchanan, and D.A. Nieuwland, pp. 179-188, Geol. Soc. Lon., 1996.

Kerr, H.G., N. White, and J.P. Brun, An automatic method for determining three-dimensional normal fault geometries, *J. Geophys. Res.*, *98* (B10), 17,837-17,857, 1993.

Kokogian, D.A., F. Fernandez-Seveso, and A. Mosquera, Las secuencias sedimentarias Triasicas, in *XII Congreso Geológico Argentino y II Congreso de Exploración de Hidrocarburos*, edited by V.A. Ramos, pp. 65-78, Congr. Geol. Argent., Mendoza, Argentina, 1993.

Kozlowski, E.E., R. Manceda, and V.A. Ramos, Estructura, in *XII Congreso Geológico Argentino y II Congreso de Exploración de Hidrocarburos*, edited by V.A. Ramos, pp. 235-256, Congr. Geol. Argent., Mendoza, Argentina, 1993.

Medwedeff, D.A., and J. Suppe, Multibend fault-bend folding, *J. Struct. Geol.*, *19* (3-4), 279-292, 1997.

Menke, W., *Geophysical Data Analysis: Discrete Inverse Theory*, 260 pp., Academic, San Diego, Calif., 1984.

Milana, J.P., and J.J. Zambrano, La Cerrillada Pedemontana Mendocina: Un sistmea geológico retrocorrido en vías de desarrollo, *Rev. Asoc. Geol. Argent.*, *51* (4), 289-303, 1996.

Mosar, J., and J. Suppe, Role of shear in fault-propagation folding, in *Thrust Tectonics*, edited by K.R. McClay, pp. 123-132, St. Edmundsbury, Bury St. Edmunds, England, 1992.

Press, W.H., S.A. Teukolsky, W.T. Vetterling, and B.P. Flannery, *Numerical Recipes in C*, 994 pp., Cambridge Univ. Press, New York, 1992.

Ramos, V.A., M. Cegarra, and E. Cristallini, Cenozoic tectonics of the High Andes of west-central Argentina (30-36° latitude), *Tectonophysics*, *259*, 185-200, 1996.

Ramsay, J.G., *Folding and Fracturing of Rocks*, 568 pp., McGraw-Hill, New York, 1967.

Sambridge, M.S., and B.L.N. Kennett, A novel method of hypocentre location, *Geophys. J. R. astron. Soc.*, *87*, 679-697, 1986.

Sandvol, E., and T. Hearn, Bootstrapping shear-wave splitting errors, *Bull. Seismol. Soc. Am.*, *84* (6), 1-7, 1994.

Sarewitz, D., High rates of late Cenozoic crustal shortening in the Andean foreland, Mendoza Province, Argentina, *Geology*, *16*, 1138-1142, 1988.

Shaw, J.H., and P.M. Shearer, An elusive blind-thrust fault beneath metropolitan Los Angeles, *Science*, *283*, 1516-1518, 1999.

Sheriff, R.E., and L.P. Geldhart, *Exploration Seismology*, 592 pp., Cambridge Univ., New York, 1995.

Stein, R.S., and R.S. Yeats, Hidden earthquakes, *Sci. Am.*, *260* (6), 48-57, 1989.

Suppe, J., Geometry and kinematics of fault-bend folding, *Am. J. Sci.*, *283*, 684-721, 1983.

Suppe, J., and D. Medwedeff, Geometry and kinematics of fault-propagation folding, *Eclogae Geol. Helv.*, *83*, 409-454, 1990.

Triep, E.G., La falla activada duranta el sismo principal de Mendoza de 1985 e implicaciones tectonicas, *Congr. Geol. Argent. Actas 10th*, *1*, 199-202, 1987.

Unruh, J.R., and R.J. Twiss, Coseismic growth of basement-involved anticlines; the Northridge-Laramide connection, *Geology*, *26* (4), 335-338, 1998.

White, N., Constraints on the measurement of extension in the brittle upper crust, *Nor. Geol. Tidsskr.*, *67*, 269-279, 1987.

White, N.J., J.A. Jackson, and D.P. McKenzie, The relationship between the geometry of normal faults and that of the sedimentary layers in their hanging walls, *J. Struct. Geol.*, *8* (8), 897-909, 1986.

Woodward, N.B., S.E. Boyer, and J. Suppe, *Balanced Geological Cross-Sections: An Essential Technique in Geological Research and Exploration Short Course Geol.*, vol. 6, 132 pp., AGU, Washington D. C., 1989.

Yilmaz, O., *Seismic Data Processing*, 526 pp., Soc. Explor. Geophys., Tulsa, Okla., 1987.

Zamarbide, J.L., and J.C. Castano, Analysis of the January 26th, 1985, Mendoza (Argentina) earthquake effects and of their possible correlation with the recorded accelerograms and soil conditions, *Tectonophysics*, *218*, 221-235, 1993.

B.A. Brooks, University of Hawaii at Manoa, Hawaii Institute for Geophysics and Planetology, POST suite 602, Honolulu, HI, 96822. (bbrooks@soest.hawaii.edu)

A. Ross, Geologisk Inst, Oster Voldgade 10, Copenhagen K, DK 1350. (ross@seis.geol.ku.dk)

E. Sandvol, Institute for the Study of the Continents, Department of Geological Sciences, Cornell University, Ithaca, NY 14853. (sandvol@geology.cornell.edu)

(Received January 13, 1999; revised January 3, 2000;
accepted February 3, 2000.)